

ACS Energy LETTERS

DECEMBER 2017 VOLUME 2 NUMBER 12
pubs.acs.org/acseneryletters

Nanoscale Imaging of Perovskites,
Batteries, and Beyond



ACS Publications
Most Trusted. Most Cited. Most Read.

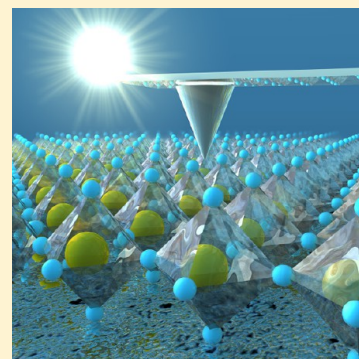
www.acs.org

Imaging Energy Harvesting and Storage Systems at the Nanoscale

Elizabeth M. Tennyson,¹ Chen Gong, and Marina S. Leite^{1*}

Department of Materials Science and Engineering, and Institute for Research in Electronics and Applied Physics, University of Maryland, College Park, Maryland 20742, United States

ABSTRACT: Our scientific understanding of the nanoscale world is continuously growing ever since atomic force microscopy (AFM) has enabled us to “see” materials at this length scale. Beyond morphology, functional imaging is becoming standard practice as new AFM-based techniques are continuously extending its capabilities. Resolving material properties with high spatial accuracy is now extremely critical as future next-generation energy harvesting and storage systems are comprised of complex and intricate nanoscale features. Here, we review recent research discoveries that implemented AFM methods to measure and determine how the electrical, chemical, and/or optical properties influence the overall device behavior. We dedicate a portion of this Review to perovskite solar cells, which are of primary interest to photovoltaic research, and highlight the remarkable progress made toward understanding and controlling their instabilities. We conclude with a summary and outlook anticipating the most pressing materials-related challenges associated with solar cells and batteries and how that will likely be overcome in the near future by nanoimaging through AFM.



Imagine gently gliding along the surface of an object with the tip of your index finger—what types of information can you obtain? Most likely, you will feel the texture (surface roughness), temperature, shape, hardness, etc. of the item. All of this information is acquired in less than 1 s by neurons firing from your fingertip to your brain. Atomic force microscopy (AFM) is analogous to this situation, except replace your fingertip by a nanoscale probe and the neuron reactions with the microscope detection system. AFM is, thus, an extremely powerful tool that probes the morphological, electrical, magnetic, mechanical, chemical, and optical properties of the sample under examination. Since its first implementation in the 1980s,¹ AFM has revolutionized our understanding of a variety of nanoscale systems,^{2,3} including materials for energy harvesting and storage, as will be presented in this Review.

AFM is undoubtedly a versatile tool to image the functionality of energy harvesting and storage materials, and its full potential has yet to be realized as new techniques will shed light on faster, dynamic processes.

In most AFM-based setups, there is a probe with a radius ranging from 1 to 100 nm that is positioned very close to or in contact with the surface of a sample, illustrated in Figure 1. The spatial resolution of AFM imaging methods is, then, primarily limited by the size of the probe. The interaction between

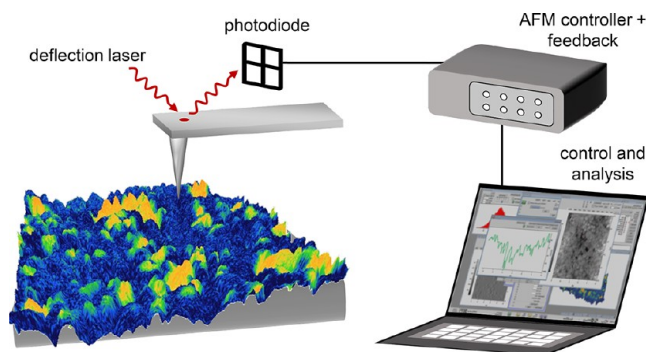


Figure 1. Principle of AFM operation. Illustration of an AFM probe scanning the surface of a textured, nonuniform sample. A laser is deflected from the back of the probe onto a photodiode, and any change in the tip–sample interaction is translated as the laser’s coordinates on the photodiode. As a consequence, the feedback system within the AFM adjusts itself accordingly. Out of scale for clarity.

the AFM tip and sample is detected by a photodiode that collects laser light deflected off of the back of the cantilever. The photodiode is calibrated with specified x – y coordinates and continuously keeps track of the laser position. Therefore, any minute movement of the probe, whether caused by a small

Received: September 28, 2017

Accepted: October 30, 2017

Published: October 30, 2017

change in sample height or electronic carrier concentration, is detected. The feedback loop system adjusts the cantilever deflection, depending on the measurement mode of interest. There are many forces and interactions, such as electrostatic, capillary, or chemical potential, that can excite the tip and/or sample causing the deflection laser's x - y coordinates to change. Beyond the surface roughness,^{4,5} properties such as the local electrical, chemical, and optical spatial variations are imaged, which will be discussed in detail later.

Here, we critically review the remarkable progress made in determining the properties and performance of materials for energy harvesting and storage by AFM through functional and correlative nanoscale imaging. The micro- and nanostructure of heterogeneous photovoltaic (PV) and battery/storage materials is well-known to influence their overall performance.^{6–8} Therefore, understanding the electrical and chemical processes that harm device operation is crucial for future renewable energy generation, conversion, and storage systems. We choose to focus on AFM methods in this Review because they encompass key desirable features such as the ability to perform measurements in *operando* conditions with 3D nanoscale spatial resolution, are nondestructive, and require very little sample preparation. Further, AFM is undoubtedly a versatile tool to image the functionality of energy harvesting and storage materials, and its full potential has yet to be realized as new techniques will shed light on faster, dynamic processes. We target selected AFM-based methods that are specifically implemented to investigate the nanoscale properties of energy conversion and storage systems that translate into device performance, such as the electrical and optical response of solar cells (through measurements of photovoltage, photon-induced current, and charge carrier lifetime) and chemical composition in batteries (e.g., electrochemical strain). In the realm of PVs, we provide an in-depth discussion of each imaging method that has been utilized to probe relevant properties of next-generation solar cells. In particular, we focus on performance mapping and perovskite dynamics as it is at the forefront of interest for scientists and engineers working on PVs. These novel scanning methods have the potential to elucidate key open questions about the physical behavior of perovskite devices. Concerning batteries and fuel cells, improvement of the current state-of-the-art energy storage technologies critically depends on the ability to control the ionic functionality and electrochemistry at the nanoscale. As an example, we discuss how electrochemical strain microscopy has been recently developed to image the Li distribution and probe reactivity upon device cycling.

1. AFM for Energy Harvesting Systems. The most promising emerging PV materials consist of microstructured semiconductors with boundaries and interfaces that can lead to undesirable nonradiative recombination of charge carriers, reducing the power conversion efficiency (η) of the device significantly below its theoretical limit.^{6,7} The applications of these heterogeneous materials, including perovskites, CdTe, Cu(In,Ga)Se₂ (CIGS), Cu₂ZnSnS₄ (CZTS), quantum dots, organics, dye-sensitized, etc., are aimed toward lower-cost and/or higher-efficiency solar markets. Often, the devices are fabricated as thin films (≤ 3 μm thickness), which can be deposited on a variety of surfaces with distinct mechanical properties, including flexible substrates. Despite the potential low cost ($\$/\text{kW}$) of these devices, it is currently not well understood how their structure affects charge carrier generation, recombination, and collection at the nanoscale.

Thus, imaging the key physical and chemical properties of these materials is crucial to their further development. In this section of the Review, we describe how AFM methods have been realized to probe the electrical, chemical, and optical properties of nonepitaxial materials for PV.

1.1. Electrical Properties. Understanding the nanoscale electrical characteristics of energy harvesting systems, such as solar cells, is the next step toward realizing devices with controlled response and, thus, enhanced performance. In AFM-based techniques, the electrical signal is the main diagnostic tool used to indicate whether the local voltage and/or current of a PV device is affected by the material's morphology and how its spatial variation compares with the average, macroscopic device response. Nanoscale electrical characterization can help answer critical, still not fully solved questions such as "How do the aggregates in perovskite thin films affect overall device morphology and performance?"⁹ "Does the lifetime of charge carriers vary as a function of incident wavelength in organic PVs?"¹⁰ and "What is the specific contribution of grain boundaries in CIGS and CdTe solar cells to the local electrical signal?"^{11,12} We review the most relevant AFM methods that have made contributions toward revealing the effect of the light-absorbing microstructure on the electronic response.

A variant of AFM to measure local voltage with nanoscale spatial resolution is called Kelvin probe force microscopy (KPFM), which we have recently demonstrated to map the open-circuit voltage in solar cells^{11,15} (a detailed discussion is presented in section 1.1.1). KPFM measures the work function difference between a conductive probe and the sample surface, termed the contact potential difference (V_{CPD}). KPFM was theorized by Lord Kelvin in 1898¹⁶ and first implemented a couple of decades ago to characterize the local electrical signal of metal and semiconductor surfaces.^{17,18} The work function (W) is the energy level difference between the vacuum and Fermi level (E_{F}). The probe, typically Si coated with a thin conductive metal layer, is assumed to have a constant W in noncontact scanning mode. In equilibrium (no light), the solar cell's W at the surface stays constant; however, in the case of nonuniform, heterogeneous materials, the work function may vary locally depending on grain orientation,¹⁹ E_{F} pinning,^{20,21} charge trapping,²² and chemical composition, among other factors. When the sample is illuminated, it generates charge carriers and is, thus, in a nonequilibrium state.

KPFM is frequently used as a diagnostic tool to image the voltage response before and after specific deposition steps, relevant for optimizing the fabrication parameters of the films. In Figure 2a, Seidel's group compared how the electrical signal of (FAPbI₃)_{0.85}(MAPbBr₃)_{0.15} (FA = formamidinium, MA = methylammonium) perovskite compounds with and without an additional (5.7 mol %) PbI₂ reacts locally when an external voltage bias (inducing ion migration) is applied, by KPFM.⁹ It was found that the V_{CPD} of the sample without the extra treatment step presents a dramatic change as a function of bias, particularly at the grain boundaries, while the V_{CPD} of the device with excess PbI₂ remains constant at both the grain interiors and grain boundaries. These observations were attributed to ionic migration suppression due to the incorporation of excess PbI₂, which in turn improves the overall electrical properties of the solar cell.

A derivative of KPFM, called either intensity-modulated or illuminated-assisted KPFM, measures the decay of the surface photovoltage (SPV), which is the subtraction between an illuminated and a dark KPFM scan in the same location.

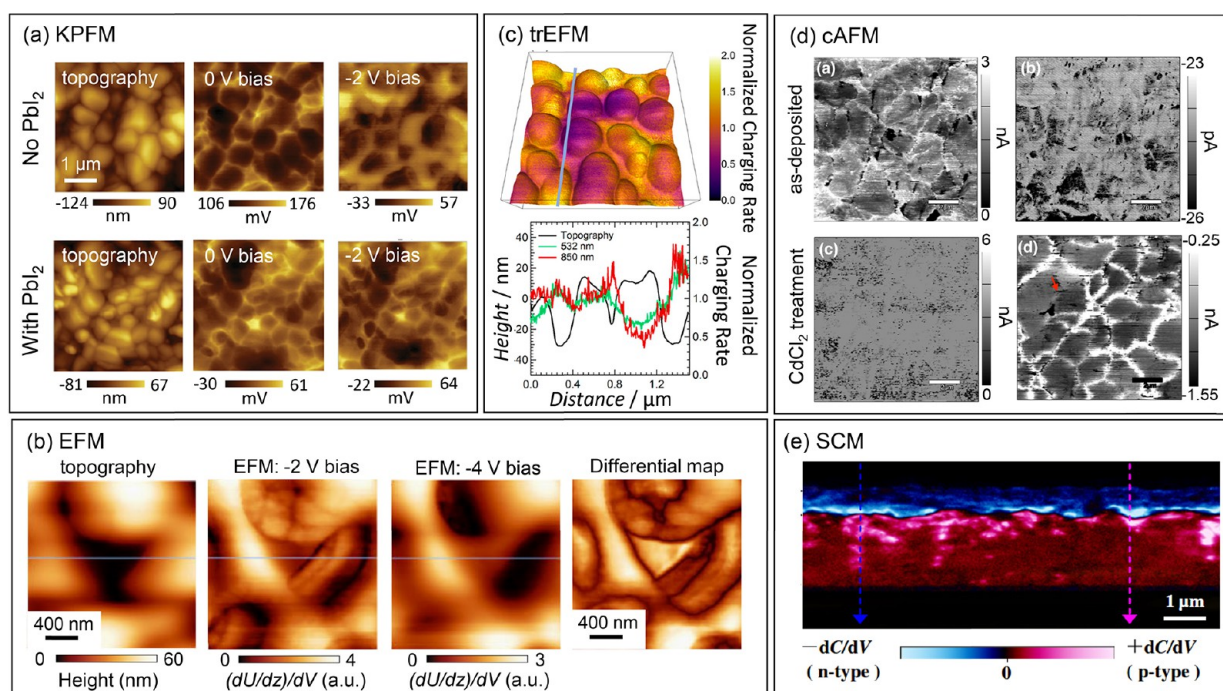


Figure 2. Nanoinaging electrical properties by AFM. (a) Topography and KPFM of two perovskite solar cells, with and without the incorporation of 5.7 mol % of PbI_2 , as a function of voltage bias. Illumination conditions: 500 nm incident light and photon flux = 0.3 kW/m^2 . Adapted with permission from ref 9, Copyright 2015 WILEY-VCH Verlag GmbH & Co. KGaA, Weinheim. (b) AFM and corresponding EFM images of a MDMO-PPV:PCBM (1:4) polymer blend thin film acquired at different applied biases. Far right: differential map of the two biased EFM maps. Adapted from ref 13, Copyright 2016 The Japanese Journal of Applied Physics. (c) Top: trEFM map overlaid on the topography in a polymer half-processed solar cell in a $1.5 \times 1.5 \mu\text{m}^2$ region. Bottom: Profile of the topography and relative charging rate acquired for two different photon excitations. Adapted from ref 10. (d) cAFM maps of the local current signal for both nonpassivated and passivated CdTe solar cells in a $10 \times 10 \mu\text{m}^2$ area. Adapted from ref 12. (e) SCM on the cross section of a CIGS solar cell defines the location of the p–n junction and qualitatively shows the density of dopants in each respective layer. Adapted with permission from ref 14, Copyright 2014 IOP Publishing Ltd.

Here, the V_{CPD} depends on the frequency of the laser pulse, and a transient SPV signal resolved on the order of submilliseconds is observed.^{23,24} The decay rate of the SPV is related to the minority charge carrier lifetime, as shown in refs 25 and 26. Briefly, when the illumination source is in OFF mode, the PV voltage decays exponentially and is proportional to $e^{-t/\tau}$, where τ is the minority carrier lifetime. These pioneering works yield insights that link the local photovoltage, lifetime, and topography, especially useful for correlating the role of the microstructure to a specific type of recombination mechanism.

Electrostatic force microscopy (EFM), of the same family as KPFM, also measures the electrical signal of the tip–sample interaction while applying a voltage to the tip in noncontact mode. The deflection of the AFM probe is linked to the electrostatic force (F_{ES}) between the sample surface and tip.^{27,28} That is, the oscillation path (z -axis) of the cantilever changes depending on the electrical charge distribution located at the sample surface. The electrostatic force is described as

$$F_{\text{ES}} = \frac{1}{2} \frac{dC}{dz} V^2 \quad (1)$$

where z is the distance between the tip and sample, C is the tip-to-sample capacitance, and V is a voltage term that encompasses all voltages flowing within the AFM experimental setup. The amount of tip deflection is related to the charge carrier density; therefore, by utilizing EFM, one can map electrical properties such as capacitance, surface voltages, or electrostatic potentials.²⁹ The capability of this technique is exemplified in Figure 2b, where the surface charge of a

poly[2-methoxy-5-(3A,7A-dimethyloctyloxy)-1,4-phenylenevinylene] (MDMO-PPV):phenyl-C61-butyric-acid-methyl ester (PCBM) polymer blend thin film is mapped as a function of external voltage.¹³ Here, Takuya's group was able to determine how the electrostatic properties of an organic PV system influence device performance. Both the permanent (addition of two EFM maps set at different voltage bias values) and field-induced (differential of two biased EFM maps) charge components were acquired. While the permanent portion of the EFM signal did not affect performance, the differential map shows sharp, dark contrasts, which could be related to charge trapping.

Time-resolved EFM (trEFM), an extension of traditional EFM, measures the charging rate by tracking the resonance frequency shift that occurs between the probe and the sample due to charge accumulation.^{30,31} Under illumination or external voltage bias, a solar cell generates electrons and holes at a specific rate. A faster charging rate implies an increase in charge buildup under the probe, shifting the cantilever frequency further away from its equilibrium resonance peak, dependent on both the incident photon energy and quantum efficiency. Each of these quantities is known for varying spatially in organic heterogeneous PV materials. Figure 2c shows a 3D topography map overlaid with trEFM data on a MDMO-PPV:PCBM (wt/wt 1:4) organic blend cast from toluene.¹⁰ The black curve denotes topography, while the green and red ones are the normalized charging rates under 532 (above bandgap) and 850 nm (below bandgap) illumination, respectively. The trEFM line scans present similar spatial

trends and, thus, are independent of the incident wavelength. This result suggests that the internal quantum efficiency of the polymer material is equal across a wide range of photon energies. Ginger's group observed that segregated regions of PCBM have lower charging rates than if the film were to have a completely uniform blend.

One way to measure the current of a PV device at the nanoscale is to probe the sample using conductive- or photoconductive-AFM (cAFM or pcAFM). Here, a cAFM probe in contact with the sample surface acts as a local electrode that collects the solar cell's dark (cAFM) and/or light-generated current (pcAFM). This mature method has been widely used to image a variety of materials for solar cells, such as perovskites,^{32–35} thin-film polycrystallines,^{12,36,37} and others.^{38–42} One pressing question that cAFM can help answer is "What is the specific role of the CdCl₂ treatment on the electrical properties of CdTe solar cells?" It has been ubiquitously demonstrated, at a macroscopic level, that the CdCl₂ improves PV performance by passivating the CdTe grains and interfaces;^{43–45} yet, resolving how it affects the local electrical signal is still not well understood. Thus, cAFM has been applied to elucidate how this extra fabrication step enhances CdTe performance; see Figure 2d.¹² Here, Rockett's group imaged two CdTe solar cells, with and without CdCl₂ treatment, under multiple external voltages using a Pt-coated Si probe. Both the top-left and bottom-right maps were obtained at a bias of +6 V, while the top-right and bottom-left were acquired at –6 V. Under positive bias the p–n junction of the CdTe solar cell experiences reverse breakdown voltage due to the geometry of the measurement. In this case, the current contrast between the grains and grain boundaries in Figure 2d is accentuated for the CdCl₂ treated sample, caused by injection of electrons into the grain boundaries from the probe. This indicates that the grain boundaries are less p-type than the grain interiors in the treated sample. While applying a negative voltage, the sample undergoes forward bias and the current flow in this regime is due to electron injection from the p–n junction into the CdTe layer. The magnitude of the current under negative applied bias is limited by the electron collection of the AFM tip and/or by the recombination of charge carriers at the back Schottky contact. While this technique is a great approach to directly map the current generated by a solar cell with nanoscale spatial resolution, much care should be taken when acquiring images as the thin conductive coating of the probe can be easily removed, producing artifacts in the electrical signal.

Scanning capacitance microscopy (SCM) maps the differential capacitance ($\delta C/\delta V$), enabling dopant concentration imaging in microelectronic systems such as solar cells. Briefly, the capacitance of a semiconductor can be tuned by applying an alternating electric field to a conductive-coated tip and is subsequently measured by tracking the third harmonic frequency of the cantilever.⁴⁶ The type of doping (n or p) can be deduced based on the sign of $\delta C/\delta V$, while the magnitude of the capacitance is based on carrier concentration.⁴⁷ Further, there has been some research effort to quantitatively link $\delta C/\delta V$ to charge carrier concentration in different types of semiconductor materials, such as Si, GaN, and others.⁴⁸ Daisnke's group imaged a cross-sectional SCM map of a CIGS solar cell, Figure 2e, showing the qualitative carrier concentration at the CdS/CIGS n–p junction.¹⁴ Both the accumulation and depletion regions were directly mapped, important for determining where the electrons and holes are generated throughout the PV films.

1.1.1. Attributing Electrical Properties to Performance. While standard electrical property mapping is an extremely informative way to gain fundamental insights about PV materials and devices, quantifying and relating nanoscale charge carrier phenomena back to device performance is a critical next step that will lead to the rational design of solar cells with high power conversion efficiencies. There has been novel research that links the acquired electrical output to a relevant solar cell parameter, namely, photovoltage and photocurrent. Our group recently modified illuminated KPFM to quantify the local open-circuit voltage (V_{oc}),¹¹ one of the most important figures-of-merit that define PV performance.⁶ For this, the AFM probe must be grounded with respect to the bottom electrode of the solar cell and the experimental setup calibrated. In this way, when both a dark and an illuminated KPFM map are acquired on the same region of a sample, and subsequently subtracted, the remaining value is the quasi-Fermi level ($\Delta\mu$). As seen in eq 2, $\Delta\mu$ is directly proportional to the V_{oc} of the PV device

$$\Delta\mu = V_{oc} \times q \quad (2)$$

where q is the elementary charge. Figure 3a shows a V_{oc} map containing two grain boundaries in a CdTe solar cell with distinct and contrasting electrical behavior. The defect highlighted on the left locally reduces the V_{oc} by 60 mV, while the grain boundary on the right acts similar to the grain interiors, maintaining a voltage response comparable to its surrounding grains. Here, we determined the quantitative contribution of CdTe grains and grain boundaries to the local V_{oc} . We also revealed local voltage variations in CIGS solar cells as high as 250 mV, demonstrating the large influence that the microstructure can have on the recombination of charge carriers, consistent with other KPFM measurements on CIGS.⁴⁹ Overall, we have demonstrated that this powerful nanoimaging approach is a universal tool to directly map the local V_{oc} of mono-, polycrystalline, and perovskite solar cell devices and works in ambient environment.^{11,15}

Quantifying and relating nanoscale charge carrier phenomena back to device performance is a critical next step that will lead to the rational design of solar cells with high power conversion efficiencies.

AFM-based techniques are often limited to imaging properties at the sample surface; however, a method recently developed, conducting tomographic AFM, maps the photocurrent in 3D, demonstrated in Figure 3b.³⁶ In pcAFM mode, a diamond-coated probe with a high toughness value iteratively etches away the top few nanometers of the surface to reveal CdTe grains and their respective photogenerated current. While this technique is destructive in the scanned region, charge carrier transport pathways previously hidden are measured. Using this method, Huey's group identified inter- and intragrain planar defects attributed to local wurtzite and zinc blende structure variations, consistent with stacking faults imaged with transmission electron microscopy (TEM) of the same sample. Further, by scanning the region under bias, grain boundaries with n-type characteristics were resolved.

1.2. Chemical Properties. Very recently, researchers have extended AFM to map the chemical information on materials

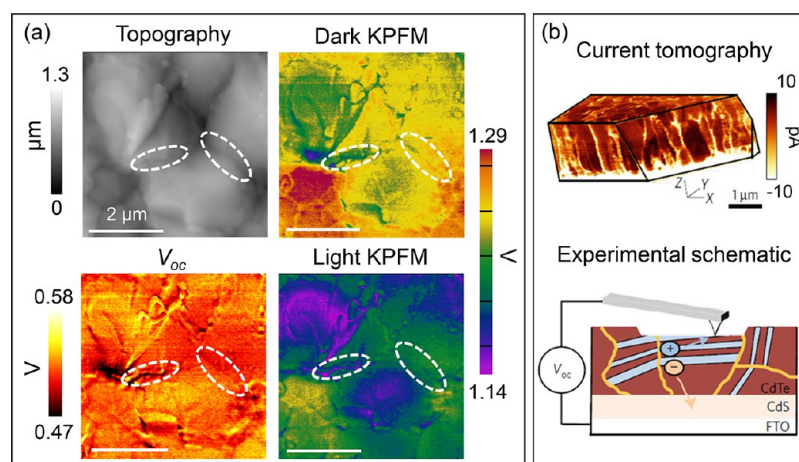


Figure 3. PV performance at the nanoscale. (a) Illuminated KPFM on a CdTe solar cell results in direct imaging of the local V_{oc} by subtracting an illuminated scan by a dark one. Adapted with permission from ref 11, Copyright 2015 WILEY-VCH Verlag GmbH & Co. KGaA, Weinheim. (b) A variant of cAFM, conducting tomographic AFM, biased near V_{oc} . A tough diamond-coated probe was used to etch away the top surface layer after each current map of a CdTe solar cell. Adapted by permission from Macmillan Publishers Ltd.: Nature Energy,³⁶ Copyright 2016.

for PV at the nanoscale.⁵⁰ Now, more than ever, identifying the elemental distribution with nanoscale spatial resolution is relevant for heterogeneous, next-generation PV technologies to improve the state-of-knowledge of crucial unanswered questions, such as “Where do the Br_3 , Cl_3 , or I_3 ions segregate in mixed perovskite materials upon illumination?”,^{51,52} “Is the non-uniform electrical response of perovskites related to variations in chemical composition?”,^{15,32} “Is it possible to chemically resolve where the different species in a block copolymer thin film preferentially accumulates/segregates?”,⁵³ “What is the primary substance limiting the electrical conductivity in polymer solar cells?”,⁵⁴ and “Are the majority of grain boundaries in CZTS thin-film solar cells of Cu-rich or Cu-poor composition?”.⁵⁵

Tip-enhanced Raman spectroscopy (TERS) is an effective method to image the chemical composition of materials.^{57–59} The experimental setup for TERS requires a high-intensity polarized light focused on the apex of a metal-coated AFM probe (e.g., Ag or Au) held ~ 20 nm above the sample surface. The interaction between the incident far-field photons and the tip induces a large electromagnetic near-field enhancement, capable of exciting Raman vibrational modes. The amplification effect is attributed to localized surface plasmons that are generated by the incident photon energy, which is usually near the resonant peak of the metal coating on the AFM cantilever.^{57,60,61} The strong excited optical field is coupled into a spectrometer, where each pixel in a TERS map corresponds to a spectrum. TERS is particularly useful when analyzing systems with inhomogeneous chemical composition distributions, such as perovskite and organic solar cells, as the agglomeration or separation of elemental compounds can deteriorate the electrical performance of the devices. Figure 4a shows the topography (top) and corresponding TERS image (bottom) of a PCBM (acceptor) and poly(3-hexylthiophene) (P3HT, donor) polymer solar cell.⁵⁴ Meixner’s group attributes the bright red feature in the center of the chemical map to a PCBM aggregate that formed on the surface of the polymer due to an unoptimized annealing step. PCBM was identified by both the Raman and photoluminescence (PL) spectra in this region, and the spatial distribution of the chemical trace was only discernible in the TERS imaging. Confocal microscopy

was attempted in the same location, and no change in the Raman signal was detected. This PCBM aggregate is responsible for the limited electron transfer observed in these polymeric solar cells, resolved by TERS measurements.

Photoinduced force microscopy (PiFM) is an emerging approach that was developed in 2010.⁶² Here, the near-field Raman signal is detected in noncontact mode. Thus, changes in the time-averaged force gradient of the tip–sample interaction are measured, rather than a spectrum.⁶³ During the experiment, one (tunable) or two lasers (of different wavelengths) are focused onto the sample; they modulate at frequencies that are selected based on the first and/or second resonance of the cantilever. The external excitation generates a unique response in the force curve that is captured by a lock-in amplifier.⁶⁴ In general, the experimental setup is compatible with bottom illumination with a high numerical aperture objective lens. The spatial resolution of the PiFM image is slightly better than the simultaneously acquired topography map because the PiFM is both excited and detected in the near-field regime. The signal-to-noise ratio of PiFM is substantially larger than the one of TERS because the latter is detected in the far-field regime. These advantages extend chemical imaging spatial resolution, which can be used to reveal nanoscale domains within composites or to determine the specific segregation regions in mixed perovskites.^{51,65} As a proof-of-concept and to demonstrate the power of this technique, Park’s group imaged a block copolymer material, poly(styrene-*b*-methyl methacrylate) (PS-*b*-PMMA), with very well-defined Raman molecular signatures, and identified each chemical compound with <10 nm resolution; see Figure 4b.⁵³ A point-by-point PiFM response spectrum is shown on the left, executed by sweeping a quantum cascade laser at the given wavenumber and recording the magnitude of the cantilever’s deflection. On the right side of Figure 4b, two PiFM images in the same location are acquired by consecutively exciting the sample at wavenumbers 1492 (for PS) and 1733 cm^{-1} (for PMMA), where both polymers are clearly resolved. Regions of PS appear brighter in the map using the 1492 cm^{-1} excitation because its near-field Raman signal is stimulating the cantilever at its resonance frequency, detected by lock-in amplification. Note that it is necessary to know the Raman spectrum of the sample under investigation before

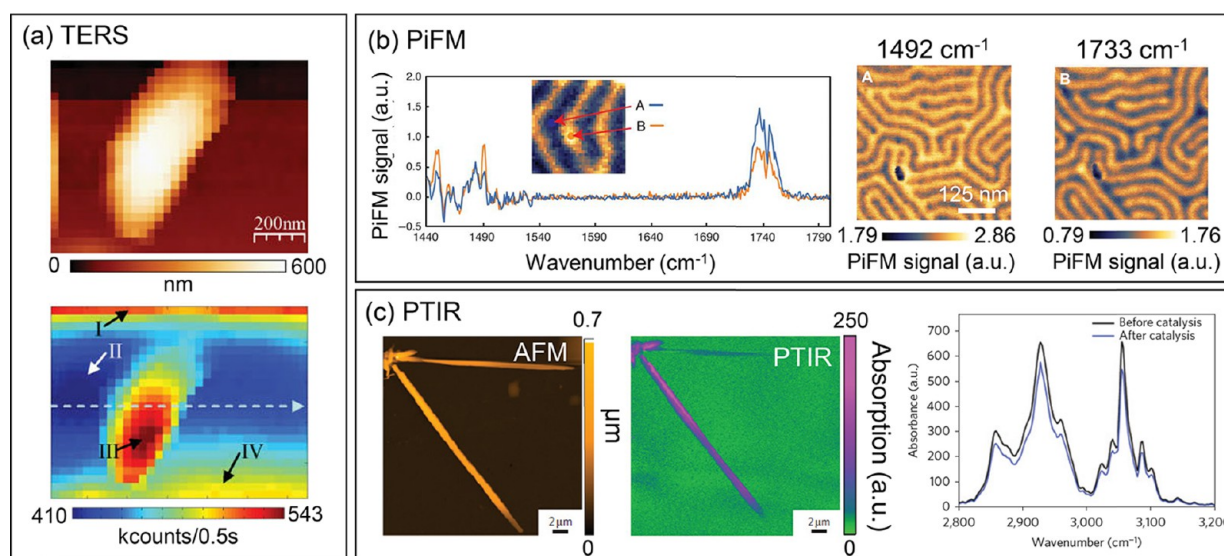


Figure 4. Nanoimaging chemical properties in solar cell materials by AFM. (a) Topography (top) and near-field TERS map (bottom) of a polymer material; a wavenumber range from 283 to 2926 cm^{-1} was integrated. Region III indicates the agglomeration of PCBM molecules. Adapted with permission from ref 54, Copyright 2010 WILEY-VCH Verlag GmbH & Co. KGaA, Weinheim. (b) PiFM images acquired at two distinct wavenumber excitations showing the two phases of a coblock polymer material. Reprinted/adapted from ref 53, Copyright the Authors, some rights reserved; exclusive licensee American Association for the Advancement of Science. Distributed under a Creative Commons Attribution NonCommercial License 4.0 (CC BY-NC) <http://creativecommons.org/licenses/by-nc/4.0/>. (c) Topography and PTIR absorption map acquired at 3054 cm^{-1} of a PDPB nanofiber. Corresponding PTIR absorption spectrum of the C–H stretching modes both before and after catalysis. Adapted by permission from Macmillan Publishers Ltd.: Nature Materials,⁵⁶ Copyright 2015.

performing PiFM to ensure appropriate selection of the excitation wavenumber. PiFM is, thus, a very promising AFM-based tool to probe materials for PV ranging from perovskites to CIGS, where local variations in chemical composition might affect carrier recombination and collection.

Photothermal induced resonance (PTIR) microscopy, or AFM-IR, combines precise IR spectroscopy with the spatial resolution of an AFM.^{66,67} Here, an external, tunable IR laser is pulsed while the AFM cantilever is in contact mode. This photon excitation induces local heating of the sample faster than the acquisition of the AFM feedback and proportional to the thermal expansion coefficient of the material. As each chemical species has a unique thermal expansion coefficient, chemical identification is attainable at the nanoscale.^{68,69} In most cases, devices or thin films under investigation are placed on top of a glass prism, where the incident light is reflected up to the sample by total internal reflection.⁷⁰ This method has been applied to resolve ferroelastic domains⁷¹ and the distribution of Cl as a function of wavelength and annealing time⁵² in perovskites. In Figure 4c, both topography and PTIR maps are presented on a UV and visible-light photocatalytic energy harvesting material, poly(diphenylbutadiyne) (PDPB).⁵⁶ Here, the conductive polymer was fabricated as a nanofiber because the photocatalytic reaction of the one-dimensional design was more efficient than its bulk counterpart. One major challenge with current light harvesters is their long-term stability; thus, Remita's group investigated PDPB, a promising material that does not require any precious metal nanoparticle co-catalyst. Nanoscale PTIR measurements demonstrated the polymer reusability as any composition degradation would be visualized in the absorption map. Further, the spectra on the right side of Figure 4c show the reproducible C–H stretching vibration modes at 3054 cm^{-1} both before and after undergoing catalysis. The overlap in the spectra indicates that there was no change in chemical composition, indicative of a stable, photocatalytic

material. This chemical mapping technique could also extend to metallic nanostructures for energy harvesting,⁷² not possible with TERS or PiFM as many metals (e.g., Ag and Au) do not have a clear Raman response.

1.3. Optical Properties. Combining the information gained from a traditional optical microscope with the spatial resolution of an AFM yields a highly impactful imaging approach that can reveal optical phenomena (i.e., reflection, absorption, and transmission) and electrical properties of materials for energy harvesting. Acquiring an optical response at the nanoscale requires a small antenna (or probe) that either excites and/or collects the near-field optical signal, entitled near-field scanning optical microscopy (NSOM or SNOM). Here, the optical information obtained is beyond the diffraction limit of light, and is restricted instead to the diameter of the NSOM probe.⁷³ Through NSOM measurements, scientists are beginning to answer questions such as “Does the migration of MA^+ and Γ^- ions in perovskites impact the index of refraction of the material?”,⁷⁴ “How can one efficiently couple far- to near-field light in order to image radiative recombination in nanoscale structures of optoelectronic devices?”,⁷⁵ “What is the spectral dependence on the local photocurrent enhancement in CdTe and CZTS grain boundaries?”,^{76,77} and “What is the correlation between the facets of GaAs polycrystals and their carrier radiative emission rate?”.^{78,79}

In near-field optics, the distance between the illumination/collection source (the NSOM probe) and the sample surface is significantly less than the wavelength of light (~ 10 nm). The theoretical description of the near-field effect was introduced in the 1920s⁸¹ but was realized more than half of a century later.^{82,83} The major experimental innovations that led to the successful implementation of NSOM are (i) depositing a thin metal coating over the NSOM probe to help guide light into the nanoscale aperture and (ii) including a feedback loop to continuously monitor/adjust the tip–sample distance.

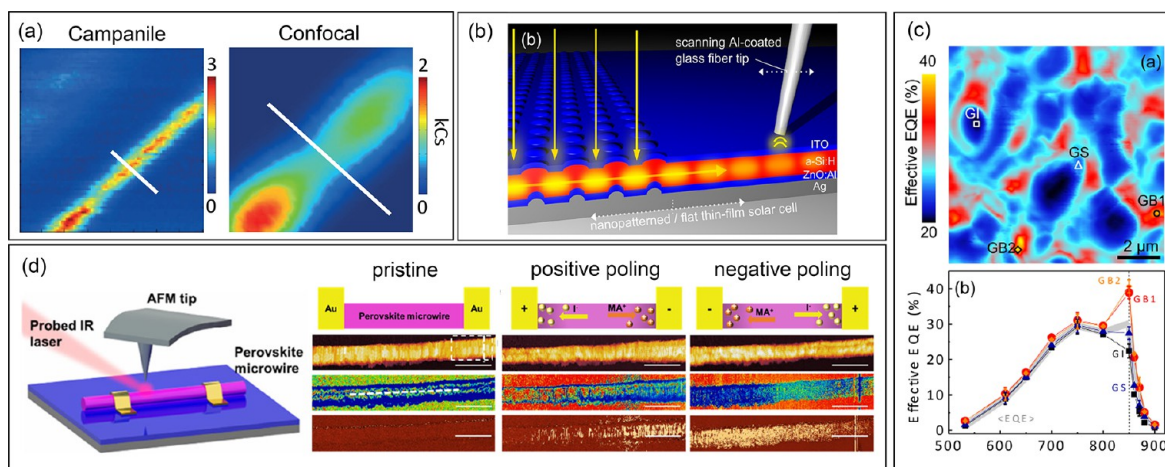


Figure 5. Nanoimaging optical properties in solar cell materials by AFM. Clockwise: (a) PL maps acquired with a near-field campanile probe and confocal objective of an InP NW in a $2 \times 2 \mu\text{m}^2$ region. From ref 75. Reprinted with permission from AAAS. (b) Illustration of NSOM in collection mode utilizing an aluminum-coated glass fiber tip to compare the near-field optical resonance of the nanopatterned region vs a flat region on an a-Si device.⁸⁰ (c) Effective EQE map measured at 850 nm (top) and average spectrally dependent EQE graph (bottom) calculated from NSOM-LBIC images of a CdTe solar cell. Adapted from ref 76. (d) Left: schematic of s-NSOM. Right: s-NSOM measurements on a perovskite microwire under different poling conditions, used to measure ion migration; the scale bar is 500 nm. In the s-NSOM amplitude maps, red = high signal and blue = low signal. Adapted from ref 74.

NSOM can be performed in multiple configurations,⁸⁴ ranging from excitation-only to reflection + collection. Below, we review the two most useful NSOM modes for solar cells, (i) collection and/or excitation and (ii) apertureless, where we discuss how these methods can be extended to determine relevant information about PV device performance.

In NSOM-PL, the probe acts as both a collection *and* an excitation source. For this, incident light passes through the small hole in the NSOM probe, and the subsequent photon emission caused by the radiative recombination of charge carriers in the solar cell is collected back through the same aperture. One example of high-efficiency, bidirectional far- to near-field coupling is presented in Figure 5a,⁷⁵ where Weber-Bargioni's group employed a new probe design shaped similar to a campanile bell tower to promote a more effective waveguide for far- to near-field coupling in a wide spectral range. In Figure 5a, NSOM and confocal PL maps of an InP NW are compared; each pixel represents the amplitude of the emission signal at 802 nm. It is immediately apparent that the image acquired with the campanile probe has much higher spatial resolution, elucidating the spatial distribution of PL within a single NW. The nonuniform emission is associated with trap-state modifications of the localized excitons, an important discovery if InP NWs are to be implemented into light harvesting devices. Since this study, there have been more NSOM-PL investigations⁸⁵ of the optoelectronic properties of solar cell materials including perovskites⁸⁶ and InGaN/GaN,⁸⁷ each presenting novel insights about the local distribution of radiative and nonradiative recombination mechanisms.

NSOM using an aperture in the collection-only configuration illuminates a large region of the sample and gathers the evanescent fields of photons propagating through the surface of the device. The NSOM probe is maintained at a distance of ~ 20 nm above the sample, close enough to allow tunneling of the guided photons. In the example shown in Figure 5b,⁸⁰ Paetzold et al. used NSOM in collection mode to resolve the near-field enhancement induced by patterned nanostructures within a solar cell as a function of both wavelength and light polarization.⁸⁰ Their results complement the

macroscopic measurements of external quantum efficiency (EQE) improvement due to the addition of metallic nanostructures.⁸⁸

One application of NSOM in excitation-only mode is light beam-induced current (LBIC) microscopy, where the photo-generated current can be spatially resolved at the nanoscale.⁸⁹ A spot size equivalent to the diameter of the aperture illuminates a solar cell and locally generates a flow of charge carriers. The photocurrent signal is typically detected by using the macroscopic contacts of the device. Resolving the light-generated current at the nanoscale is relevant when the feature size that composes a solar cell material is of a similar dimension, e.g., grain boundaries.⁷⁷ In Figure 5c, spectrally dependent NSOM-LBIC is applied to a CdTe solar cell.⁷⁶ Nanoscale spatial variations of the EQE (calculated from photocurrent measurements) at grain boundaries (GBs), grain interiors (GIs), and grain sides (GSs) were measured. Overall, Leite et al. found that GBs generate more photocurrent, hypothesized to be a local reduction in bandgap. One advantage of this optical technique over pAFM is that it is performed in noncontact mode. Thus, contact artifacts from the tip are reduced. However, the signal-to-noise ratio is substantially lower in NSOM-LBIC, and more sensitive current detectors are required.

Apertureless NSOM or scattering-NSOM (s-NSOM) follows similar operating principles as the collection-only mode, i.e., excitation uses far-field light and the optical response from the sample is collected in the near-field.⁹⁰ However, here, the probe is not hollow but instead a sharp, metallic tip (most cases an AFM probe) kept < 20 nm from the illumination spot. The apex enhances and disperses the near-field interaction induced by the incident light occurring at the sample surface, and the signal is then acquired with far-field detectors. To further increase the near-field enhancement effect, it is suggested to use an AFM probe that is coated with a thin layer of Au.⁹¹ Because in s-NSOM the tip no longer wields an aperture, the spatial resolution is equivalent to standard AFM. As previously mentioned, ion migration in perovskite materials is hypothesized to induce instabilities and degradation in the overall electrical performance. In Figure 5d, Bao's group implemented

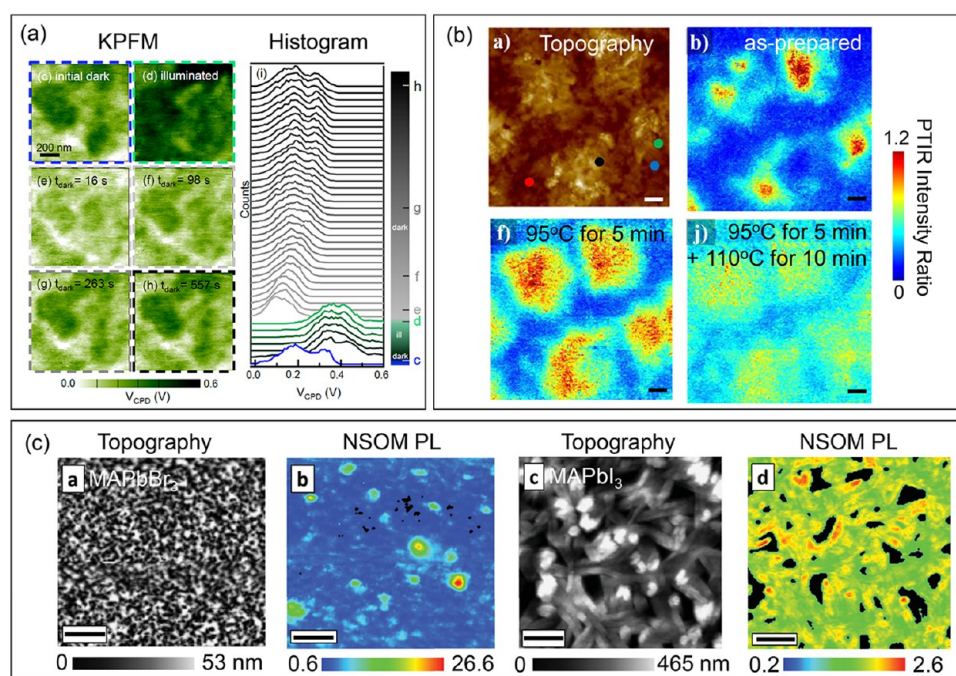


Figure 6. Imaging electrical, chemical, and optical dynamics in perovskite solar cells by AFM. (a) Sequence of fast KPFM on a perovskite solar cell under dark and illuminated conditions; each map takes 16 s. Right graph shows voltage histograms for 42 fast KPFM maps.¹⁵ (b) Topography and three PTIR maps measured at different annealing temperatures of a thin-film perovskite, where the blue regions of the map refer to high Cl concentration; scale bar is 1 μm . Adapted from ref 52. (c) NSOM topography and simultaneous PL images of two perovskite compositions, MAPbBr₃ and MAPbI₃; scale bar = 4 μm . Reproduced with permission.⁸⁶ Copyright the authors, published under CC-BY 4.0 license 2015.

apertureless NSOM to nanoimage, in situ, how the electric-field poling direction of a perovskite device influences MA⁺ and I⁻ ion migration.⁷⁴ A microwire was used to isolate and confine the direction of the ions. Near-field optical maps were obtained under mid-IR (11.7 μm) illumination to map the index or refraction and free-charge carrier distribution. On the left of Figure 5d, an illustration of the experimental setup is shown. The top portion of the right three images displays a schematic of the observed phenomenon occurring in the microwire under pristine (no applied voltage), positive poling (+10 V), and negative poling (-10 V) conditions. The topography, near-field optical amplitude, and phase images under these three conditions are presented for comparison. According to the topography maps, the perovskite material expands in the poling direction, which is also in the same orientation as the migration of the MA⁺ ions. The authors calculate that the material expansion is 4.4%; the measured shrinking–swelling effect in the perovskite structure could be one source of device degradation. Further, the near-field amplitude (here, representing the local carrier density) response is uniform under pristine conditions, but during poling, the distribution of charge carrier changes: MA⁺ ions accumulate near the negative side, and I⁻ shifts toward the positive electrode, possibly generating a temporary p–i–n junction. In the near-field phase maps (related to the perovskite’s refractive index), the negative electrode has a much larger signal, indicating a decrease in absorption due to swelling of the perovskite. Although very informative, this microscopy method suffers from high background noise due to the far-field excitation. Therefore, double lock-in or other background-suppression methods should be implemented to extract the near-field signal.⁸⁴

2. Probing Dynamic Processes in Perovskite Solar Cells. Due to the high interest in perovskites for energy harvesting,

this section of the Review is dedicated to cutting-edge research that investigates the electrical, chemical, and/or optical properties of these intriguing materials with nanoscale spatial resolution. With promising, single-junction power conversion efficiencies > 22%⁹² and a new record tandem perovskite/Si solar cell of 23.9%,⁹³ the prospect for commercializing this PV technology is approaching fruition. Moreover, there has been a recent article by Nazeeruddin’s group announcing a 1 year stable perovskite solar cell,⁹⁴ indicating that our ability to optimize and control these complex materials is increasing. Yet, there are still many challenges that lie ahead, and we are continuing to discover answers to important scientific questions such as “Can we capture the real-time effects of light illumination on the local V_{oc} of perovskites?”,¹⁵ “How do the radiative recombination distributions of charge carriers in MAPbI₃ vs MAPbBr₃ perovskite compounds differ?”,⁸⁶ “Are Cs-containing triple-cation perovskites more stable than conventional ones?”,^{95,96} “What is the role of humidity on the perovskite local electrical response?”,^{97,98} and “What are the perovskite material options that are stable upon illumination?”.^{99,100}

Perovskite solar cells experience performance instabilities caused by transient processes upon material illumination¹⁰¹ and exposure to humidity and oxygen.^{102,103} Imaging these dynamical events at relevant length scales has become an important next step toward identifying stable materials and devices. Rapid temporal mapping will likely elucidate the transport of charge carriers after excitation, spatially identifying where trap states are located. In Figure 6a, our group measured the real-time, photoinduced voltage response of a MAPbI₃ perovskite solar cell before, during, and after illumination with fast KPFM.¹⁵ Each KPFM map (left of image) was acquired in 16 s (2 orders of magnitude faster than conventional methods); therefore, it was possible to capture how the electrical signal

changes as a function of time. Immediately after the light was turned off, the photogenerated voltage ceased. However, the charge distribution was very different from the initial dark scan, as seen by comparing both the KPFM map and the voltage histograms (right side of panel). In fact, the perovskite's electrical performance remained out of equilibrium for 9 min, until finally stabilizing and returning to its initial dark conditions. While perovskite performance instability on the time scale of several minutes has been observed macroscopically,¹⁰⁴ by imaging with nanoscale spatial resolution, two distinct regions with contrasting voltage decay rates were found to coexist within a single MAPbI₃ grain, resulting from ion migration.¹⁵ The next step is to identify the relationship between this dynamic electrical response with local chemical composition variations.

Mapping the local elemental distribution in perovskites is of major interest for the PV community to help determine where ions are segregating and/or migrating. For example, in Figure 6b, a MAPbI_{3-x}Cl_x sample is annealed in situ and the AFM (top left) and PTIR signals are acquired during each thermal step. By identifying the PTIR proportion between high and low incident photon energies, local changes in the perovskite bandgap are distinguished. It is well understood that the addition of Cl increases the bandgap energy of the MAPbI₃; therefore, regions of high Cl concentration are discerned (blue in the PTIR maps; red indicates Cl-poor areas). Local increases in bandgap in the “as-prepared” sample as high as 0.3 eV were measured. However, upon further annealing, the bandgap continuously decreases, indicating that Cl content is reduced with temperature, likely caused by MACl sublimation. Additional spectrally dependent PTIR imaging with high spatial resolution on the wide variety of perovskite materials would be extremely informative, particularly to determine the role of absorption of different elements causing the instabilities of solar cell efficiency. Recently, a novel AFM-based chemical imaging method called peak-force infrared microscopy mapped the distribution of methylammonium in a MAPbBr₃ nanocrystal.¹⁰⁵

To image the radiative recombination centers in perovskite materials, Deschler's group implemented NSOM-PL on both MAPbI₃ and MAPbBr₃ thin films. Figure 6c displays the simultaneously acquired topography and PL maps for each sample. The sample containing Br₃ has a more homogeneous morphology, while the I₃ film has “needle-like” features with 25% of the scanned region comprised of voids. The PL signal shows localized hot spots (2 orders of magnitude increase) in the Br₃ sample that are not correlated with the topography. However, the I₃-containing thin film displays some PL variation, but the brighter regions are not nearly as dramatic as those in the Br₃ one. Their results, in combination with time-resolved PL measurements on the same samples, revealed that regions of high radiative recombination for both thin films have slower charge carrier decay rates. The authors concluded that the areas with higher PL emission are decoupled from the low PL regions through either a slow diffusion process or energy barrier that prevents the charge carriers from moving laterally in the perovskite layer. It is also hypothesized that higher luminescent sites are regions of enhanced structural order and better crystalline quality. AFM-based methods are vital for advancing the state-of-knowledge of the dynamic responses of perovskites when exposed to an ambient environment, where measurements prior to full device development are extremely important for the screening and classification of stable alternatives. Thus,

we offer our view of future directions for perovskites in the final section of this Review.

3. AFM for Energy Storage Systems. This section discusses how AFM methods have been implemented to advance the understanding of energy storage devices, mainly batteries and fuel cells. To access the energy harvested from intermittent renewable resources across the entire day, there is a demand to integrate PVs with batteries.^{106,107} The further development of long-lasting and high-capacity energy storage technologies necessarily entails the study of these systems' electrochemical

AFM-based methods are vital for advancing the state-of-knowledge of the dynamic responses of perovskites when exposed to an ambient environment, where measurements prior to full device development are extremely important for the screening and classification of stable alternatives.

behavior. Progress has been made to investigate the ion migration and chemical reactions for each active component and at the surface/interfaces of batteries using X-ray spectroscopy^{8,108} and electron microscopy.^{109–111} Yet, comprehensive investigations detailing how the structure influences the electrochemical functionality at the nanoscale are still intangible; therefore, an in situ SPM platform conducted under real working conditions will guide the community toward reliable, next-generation energy storage technologies.

Comprehensive investigations detailing how the structure influences the electrochemical functionality at the nanoscale are still intangible; therefore, an in situ SPM platform conducted under real working conditions will guide the community toward reliable, next-generation energy storage technologies.

3.1. Rechargeable Batteries. As the particle size composing the electrodes is typically below 1 μm,^{112,113} conventional characterization techniques, such as electrochemical impedance spectroscopy, only measure the average functional behavior. AFM-based methods can simultaneously detect the morphology and other material properties at the nanoscale; therefore, it has been adapted to investigate the electrochemistry of LIBs, among other battery technologies.¹¹⁴ Some dynamical processes in batteries include (i) ion and electron transportation in both electrodes, (ii) ion migration in electrolytes, and (iii) reactions at the electrode/electrolyte interfaces. Monitoring each active layer will require the implementation of state-of-the-art characterization tools with high spatial resolution. Here we review works that contributed toward answering the key questions in energy storage, such as “What is the correlation between fast ion diffusion and grain morphology in Li-containing cathodes?”¹¹⁵ “Is it possible to precisely control the chemical composition of the electrodes during lithiation/delithiation to suppress undesired reactions?”¹¹⁶ “Can we

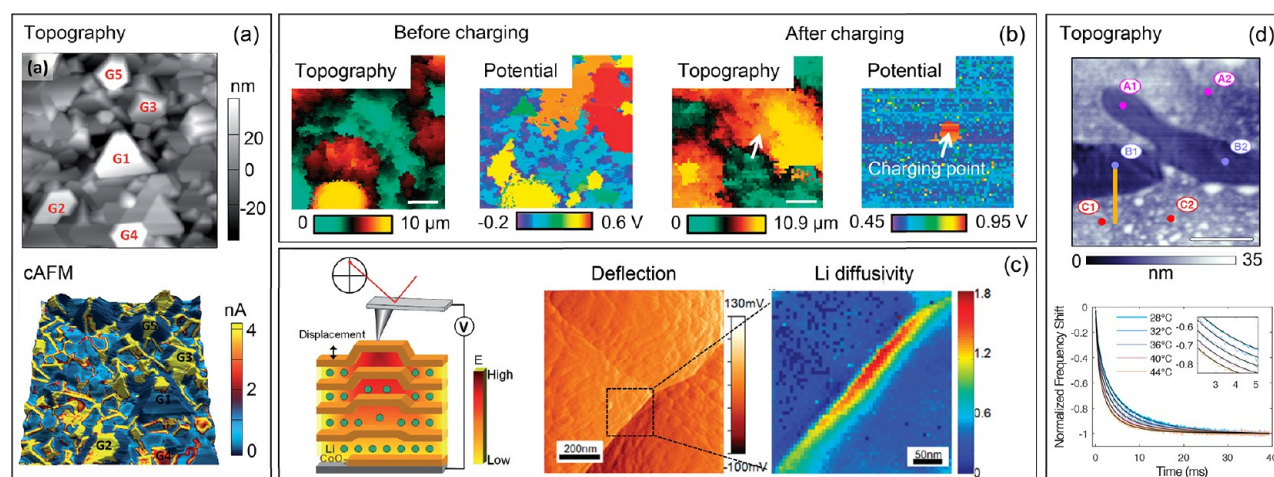


Figure 7. Imaging batteries at the nanoscale. (a) Topography and current obtained by cAFM on a $\text{Li}_{1.2}\text{Co}_{0.13}\text{Ni}_{0.13}\text{Mn}_{0.54}\text{O}_2$ cathode material. The scan size is $1.5 \times 1.5 \mu\text{m}^2$. From ref 115, Published by The Royal Society of Chemistry. (b) Topography and potential maps simultaneously acquired on a LiFePO_4 electrode through SECCM before and after charging. The charged region is indicated by a white arrow. The scanned area is $25 \times 25 \mu\text{m}^2$. Adapted with permission from Macmillan Publishers Ltd.: Nature Communications,¹¹⁶ Copyright 2014. (c) Left: Schematic of ESM measurement on an electrode, where the Li ions are represented by green dots.¹¹⁴ Reprinted with permission from Elsevier, Copyright 2011. Right: ESM images show the deflection and the Li ion diffusivity signals on a Si anode. Adapted from ref 117. (d) Topography of a LiFePO_4 cathode and plot of the resonance frequency shift vs time for different temperatures acquired at position A2; the scale bar is $2 \mu\text{m}$. The curves represent the electric field decay and are fitted to extract the effective time constant of the ionic transport within the cathode. Adapted from ref 118.

determine where high Li ion diffusivity occurs in the electrode to engineer a battery with enhanced performance?”^{114,117} and “How does the local chemical composition effect the kinetics of Li in LiFePO_4 cathodes?”¹¹⁸

cAFM has been implemented to investigate the electronic conductance of GBs in batteries as it is able to simultaneously record the topography and current signal that passes between the tip and the sample, as discussed in section 1.1. Zeng’s group¹¹⁵ applied cAFM to measure the conductivity of GBs and grain interiors of a high-capacity cathode $\text{Li}_{1.2}\text{Co}_{0.13}\text{Ni}_{0.13}\text{Mn}_{0.54}\text{O}_2$ (280 mAh g^{-1}). They revealed a higher conductivity in the majority of GBs than inside of the grain (see Figure 7a). However, they distinguished five grains (marked as G1–G5) with lower current and conductivity along their GBs, resulting from the loss of interconnection with the microstructure due to their relatively higher position (i.e., brighter regions in the topography map).

As an emerging and powerful technique, scanning electrochemical cell microscopy (SECCM) is able to image the topographical and voltammetric signals simultaneously,^{119,120} thus giving insight into the electrochemistry through mapping the electrodes in LIBs.¹¹⁶ Briefly, SECCM implements a pipet probe filled with an electrolyte solution and a quasi-reference counter electrode (QRCE). The QRCE is biased to generate a direct current (DC) flowing through the meniscus of the electrolyte at the end of the pipet, which is brought close and oscillates perpendicularly to the sample. The modulation periodically alters the contacting volume of the meniscus with the surface, creating an alternating current (AC) between the probe and the sample, and uses as a set point to maintain contact. Meanwhile, the DC signal is recorded during the experiment to provide critical information about the electrical and chemical properties. Takahashi’s group visualized electrochemical phenomena with a resolution of $\sim 100 \text{ nm}$ using SECCM on a LiFePO_4 cathode,¹¹⁶ as shown in Figure 7b. They filled the nanopipette with LiCl electrolyte and used the Ag/AgCl electrode as the QRCE. When the meniscus was in contact with

the sample (LiFePO_4), an AC signal of 2 pA was generated and the corresponding tip height was recorded as a reference for the topography mapping. To image the voltage using SECCM, the applied bias of the QRCE was regulated to equilibrate the current response from the sample to the pipet. A uniform voltage ($0.4\text{--}0.6 \text{ V}$, red in potential map) was observed on the pristine LiFePO_4 region (before charging). Subsequently, they utilized the meniscus of the electrolyte to locally charge (i.e., delithiate) the electrode and map the surface potential. A high-voltage point of around 0.8 V was measured, demonstrating the oxidation location of Fe^{II} to Fe^{III} in the cathode after charging, Figure 7b. The ability to precisely control the local redox state and chemical composition through lithiation/delithiation may reveal ion migration processes at the nanoscale. Further, combined with electron backscattering diffraction, SECCM could clarify the effect of grain orientation on electrochemical activities during battery cycling.

Electrochemical strain microscopy (ESM), developed this decade by Kalinin’s group,¹²¹ detects the local surface displacement/strain after applying a high-frequency bias using SPM on the electrode of a battery. The external voltage triggers the rearrangement of Li ions within the electrode and changes the molar volume of the embedded materials, leading to a surface displacement that is detected by the AFM tip;^{121,122} see the schematic in Figure 7c. Using ESM, Balke and colleagues measured the strain rather than the current, directly detecting ionic and electrochemical processes in Si nanoparticles.¹¹⁷ For comparison, ESM can distinguish a strain as small as 10% from lithiation/delithiation; however, the current signal from this electrochemical transformation would not be recognized. As an example, the current required to delithiate LiCoO_2 into $\text{Li}_{0.5}\text{CoO}_2$ (and generate a 10% strain) for a $20 \times 20 \times 20 \text{ nm}^3$ LiCoO_2 particle is 1.3 fA for 1 s, where theoretical capacity = 275 mAh/g ,¹²³ density = 1.68 g/cm^3 , and molar volume = 97.87 g/mol for LiCoO_2 . This value is ~ 3 orders of magnitude lower than the sensitivity of current-based AFM methods.

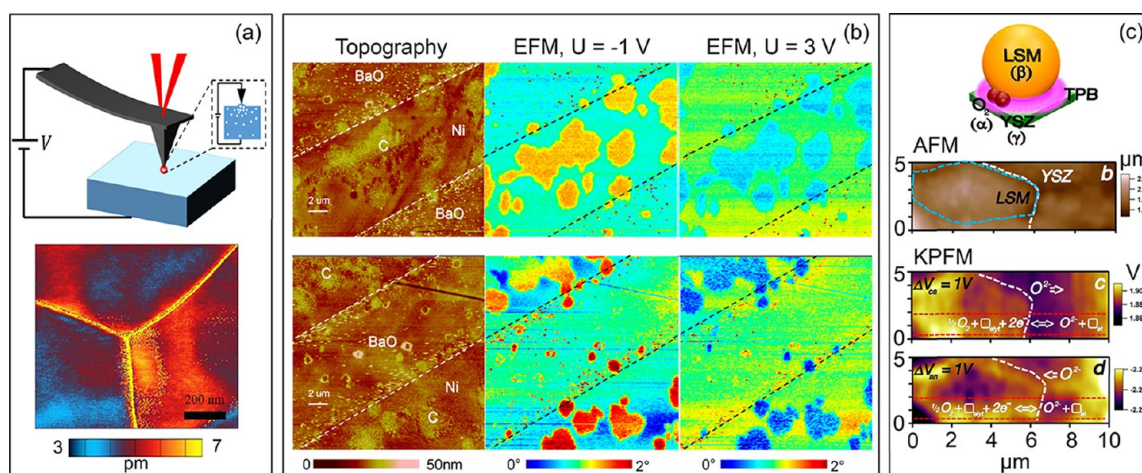


Figure 8. Nanoimaging of fuel cells. (a) ESM schematic (out of scale for clarity) and amplitude map for Sm-doped ceria demonstrating that the grain boundaries have higher ionic conductivity than the grain cores.¹²⁹ Adapted with permissions from the authors, published under CC-BY 4.0 license 2017. (b) Topography and corresponding EFM phase maps under two biases of Ni–BaO anodes showing C deposition (indicated by a warm color in the negative bias images and cool color for positive bias) mainly occurring in the region of Ni. Adapted from ref 130. (c) Illustration of the triple phase boundary (TPB) for an oxygen ion and the LSM–YSZ interface. Topography and KPFM images of the TPB at 600 °C under different polarizations (1 V_{ca} for cathodic polarization and 1 V_{an} applied for anodic). The direction of oxygen ion migration at the interface is labeled. Adapted from ref 125.

ESM voltage spectroscopy is well-equipped to determine the Li ion diffusivity at the nanoscale.¹²⁴ Typically, 2 ms DC voltage pulses, with a 2 ms relaxation time between each one, are applied with an amplitude sweep between ± 15 V. The electrochemical strain is recorded after each pulse during the experiment. By optimizing the frequency of the sweeping voltage pulses to the Li ion diffusion time, ESM directly maps the migration of ions as this response can only be attributed to the movement of Li atoms (in LIBs). Figure 7c demonstrates ESM voltage spectroscopy on a Si anode, where the measured area includes a GB. The Li diffusion map shows that the GB has a higher ion diffusivity than that inside of the grain, in agreement with cAFM results.¹¹⁵ Overall, ESM provides insight into ion diffusion with extraordinary spatial resolution for solid-state materials. Revealing these regions at such small scales could now identify failures within LIBs because local volume expansions or microstructural cracks in high-capacity anodes (e.g., Si or Ge) can be resolved.

Electrostatic force spectroscopy (analogous to EFM in section 1.1) is implemented on a LiFePO₄ cathode to resolve the different ionic hopping processes of Li.¹¹⁸ Here, a step potential is applied between the AFM probe and the sample, inducing a redistribution of ions. Grutter's group monitors the resonant frequency of the cantilever after applying an external bias; the tip's eigenmode is continuously decreasing due to the reduction of the electric field directly under the AFM tip; see Figure 7d. The electric field decay is fit to eq 3

$$\phi(t) = \exp[-(t/\tau^*)^\beta] \quad \text{for } t > t_c, 0 < \beta < 1 \quad (3)$$

where t represents time, τ^* is the effective time constant, β is the stretching factor, and t_c is the cutoff time (on the order of picoseconds). τ^* is a function of both temperature and activation energy; therefore, by measuring the cantilever frequency shift under different temperatures, the energy barrier for Li ionic hopping is experimentally determined (verified by their density functional theory calculations). This result distinguishes the Li ion activation energy barriers for both bulk material and

single Li hopping sites, thus correlating the structural and transport properties of LiFePO₄ cathodes.

3.2. Fuel Cells. For fuel cells, the dimensions of the electrochemical reactions are at the micron/submicron level.^{125,126} Thus, AFM techniques have been extended to access the local electrical properties and investigate the cell functionality^{127,128} to answer questions such as “Can we resolve regions with high ion diffusivity at the nanoscale?”,¹²⁹ “What are the new materials formed on the surface of anodes in solid oxide fuel cells (SOFCs)?”,¹³⁰ and “How can one map the potential distribution at the electrode/electrolyte interface for SOFCs under real operation conditions?”¹²⁵

Li's group¹²⁹ experimentally imaged the ion diffusion in a Sm-doped ceria fuel cell material by ESM; see the top of Figure 8a for an experimental schematic. The map (bottom of Figure 8a) shows larger strain at a triple-junction GB, indicating that there is an accumulation of ions at the interfaces. The authors then used a computational approach to model the ESM signal and a spectroscopy hysteresis curve in the same region to deconvolute the strain contribution from either ion concentration or diffusivity. They found that the strain response has a higher dependency on the local ion diffusion.

EFM, detailed in section 1.1, has also been used to analyze the nucleation processes that occur on the surface of electrodes in SOFCs. Bottomley and co-workers investigated C formation on a Ni anode during the early stages of cell operation.¹³⁰ They deposited BaO nanoclusters through polymer patterning onto an anode surface and mapped the subsequent BaO–Ni interface (topography in Figure 8b). The EFM phase maps identified the existence of C patches by showing a stark color contrast between the C and the anode composition, Figure 8b. As expected, the phase of C shifted after inverting the sign of the external applied bias. They revealed that C accumulates only on regions with no BaO coverage, suggesting that BaO suppresses the C growth and maintains active reaction sites. These results demonstrate that surface modifications on the Ni anode could potentially stabilize fuel cell performance.

Bonnell's group performed in situ KPFM (see section 1.1) to quantitatively determine the local V_{CPD} of a lanthanum

strontium manganite—yttria-stabilized zirconia (LSM–YSZ) interface at typical operation conditions: temperature = 600 °C and $P_{\text{O}_2} = 0.001$ atm.¹²⁵ Figure 8c shows the topography and KPFM maps at the TPB (white dashed line), illustrating the LSM grain at the interface (circled in a blue dashed line) with an inhomogeneous voltage distribution. Under both cathodic (ΔV_{ca}) and anodic (ΔV_{an}) polarizations, the potential at the center of the grain is lower, indicating a surface-mediated process dominating the ion transport at the TPB. This observation agrees with typical LSM behavior for low overpotentials ($\Delta V_{\text{ca}} = \Delta V_{\text{an}} = 1$ V).¹³¹ A primary parameter that determines the energy required to produce a current across the LSM–YSZ interface is termed ΔG_{R} —the change of the activation barrier from equilibrium. The researchers quantified $\Delta G_{\text{R}} = 1\text{--}2$ kJ/mol through eq 4

$$\Delta G_{\text{R}} = \alpha z F \eta_{\text{act}} \quad (4)$$

where α is the charge-transfer coefficient, z is the number of redox equivalents in the reaction ($z = 2$), F is Faraday's constant, and η_{act} is the activation potential (measured during KPFM). This work demonstrated quantitative nanoscale imaging of the electrical properties in SOFCs at a critical interface under *operando* conditions for the first time.

4. Summary and Future Directions. In this Review, we presented selected AFM methods that led to recent discoveries related to the electrical, chemical, and optical responses of materials and devices for energy harvesting and storage. Revealing the fundamental properties of these systems is crucial to increase our understanding of the underlying mechanisms that define device performance at the nanoscale.

Ultimately, we envision that high spatial resolution investigations will lead to the redesign of materials with improved performance, as well as devices.

Ultimately, we envision that high spatial resolution investigations will lead to the redesign of materials with improved performance, as well as devices. In this final section, we provide an outlook of how AFM can be further implemented to address pressing problems in materials for PVs and energy storage. First, we speculate how fast AFM methods could be used to help elucidate the role of the ambient environment on the degradation of perovskites. Second, we discuss the need for advancing NSOM-based methods, which, to date, are not widely implemented. Measurements using NSOM are particularly relevant to tackle open questions in polycrystalline PVs. Third, we consider how novel instrumentation could enable in situ AFM to probe battery operation under extreme conditions.

Nanoscale mapping of performance through KPFM and cAFM can potentially deconvolute the role of humidity, oxygen, illumination, bias, and temperature on perovskite degradation, including their effect on both grains and grain boundaries. These measurements are likely to redefine the design of solar cells using conventional and emerging perovskites, considering their contact interfaces. We anticipate the nanoimaging of perovskites through fast AFM techniques, such as heterodyne-KPFM,^{6,15,132} KPFM G-mode extension,¹³³ or 2ω D-KPFM,¹³⁴ to elucidate their dynamic electrical behavior at relevant length scales, critical to identify the driving forces behind its instabilities. In particular, we expect researchers to correlate the changes in the optoelectrical properties (photovoltage,

Nanoscale mapping of performance through KPFM and cAFM can potentially deconvolute the role of humidity, oxygen, illumination, bias, and temperature on perovskite degradation, including their effect on both grains and grain boundaries. These measurements are likely to redefine the design of solar cells using conventional and emerging perovskites, considering their contact interfaces.

photocurrent, and PL) with possible chemical composition variations through correlative microscopy (KPFM + cAFM + PiFM) on the very same grains. AFM experiments where one can elucidate the effects of ambient environment on the local electrical and optical properties will probably focus on correlative microscopy, in order to define how each parameter affects charge carrier generation, recombination, and collection, all critical for device performance. We also expect NSOM-PL, KPFM, and TERS to help us identify which perovskite compositions are stable under illumination. While extensive effort has focused on determining the ideal synthesis parameters for optimized device performance, substantial work lies ahead to identify what triggers ion migration and/or material segregation upon sample illumination and exposure to ambient conditions. This class of material has ~ 100 options;⁹⁹ thus, measurements on thin films will accelerate a high throughput and effective material selection, prior to device processing development.

Concerning polycrystalline materials for PVs, direct measurements of light–matter interactions through underutilized NSOM-based techniques are critical for tackling relevant open questions. For local optical measurements, better NSOM probes are being designed and engineered to optimize the far-to near-field light coupling as the current transmission loss is still 3–6 orders of magnitude.^{135,136} More efficient probes will allow for mapping on a broader variety of low-emission materials, including CIGS and CZTS. NSOM-PL will further impact polycrystalline GaAs fabrication¹³⁷ as the dependency of radiative recombination on different types of grain facets could be resolved. We also anticipate KPFM measurements combined with scanning electron microscopy to become more common,¹³⁸ where one can correlate, in situ, the electrical response of grains and grain boundaries with their crystalline orientations. To probe the p–n junction in inorganic solar cells, such as CdTe and CIGS, KPFM and cAFM should be applied in the cross section after cleaning the sample in an oxygen-free environment, to prevent surface recombination due to the material's exposure to air. For that, we suggest operating the AFM inside of a glovebox, where the samples can also be cleaved.

For energy storage devices, we foresee the development of advanced AFM systems to allow in situ characterizations of chemical, electrical, and electrochemical behaviors of batteries and fuel cells. For this, innovative environmental cell stages and cycling accessories will be integrated into an AFM to scan the sample while cycling. The advantages of in situ analysis are (i) eliminating sample transfer and (ii) preventing contamination due to air and/or moisture exposure. It is especially necessary to access the SEI formation and possible degradation,¹³⁹ both locally and during cycling, because such information

is time-sensitive and often hard to validate by ex situ methods. Besides cycling capabilities, environmental cells will need a temperature controller that mimics *operando* conditions. The working temperature is -35 – 55 °C for batteries¹⁴⁰ and >500 °C for SOFCs;¹²⁷ therefore, two distinct cells or one cell with unprecedentedly wide temperature ranges would be required. Further, a novel SPM instrumentation that can fully operate when the sample is under extreme conditions (high temperature and pressure) will enable the assessment of battery functionality for reliable, next-generation energy storage. We anticipate the combination of chemical and ion diffusion imaging, e.g., TERS and ESM, on the same region as the relationship between the chemical composition and electrochemistry for multicomponent electrodes¹⁴¹ is still under pursuit. In the future, ESM in conjunction with nanoscale structural studies, such as synchrotron X-ray nanodiffraction,¹⁴² will provide the crystal orientation of materials with high ion diffusivity for either battery or fuel cell applications. Ultimately, this correlative microscopy approach will describe the intricate relationship between the structural, chemical, and electrochemical properties for materials used in energy storage devices at the nanoscale.

In the past 3 decades, AFM has become the standard characterization tool to image the morphology of a specimen. In the years following its conception, scientists have modified the instrumentation to image beyond its typical measurement mode, and unleashed an array of new research opportunities to map other material properties. We have no doubt that novel adaptations will continue to develop, as speculated above. It is all at the tips of our fingers!

AUTHOR INFORMATION

Corresponding Author

*E-mail: mleite@umd.edu.

ORCID

Elizabeth M. Tennyson: 0000-0003-0071-8445

Marina S. Leite: 0000-0003-4888-8195

Notes

The authors declare no competing financial interest.

Biographies

E. M. Tennyson is currently a Ph.D. student in the Department of Materials Science and Engineering and in the Institute for Research in Electronics and Applied Physics (IREAP) at the University of Maryland—College Park. She received her B.S. in Physics from the University of Wisconsin—La Crosse in 2012. Her research focuses on the nanoscale characterization of perovskites and CIGS for photovoltaics.

C. Gong is a Ph.D. student in the Department of Materials Science and Engineering at the University of Maryland and in the Institute for Research in Electronics and Applied Physics (IREAP), College Park. He received his B.S. in Materials Science and Engineering from Shandong University, China in 2013. His research focuses on the fabrication and characterization of metals and metallic alloys for energy harvesting and storage.

M. S. Leite is an assistant professor in the Department of Materials Science and Engineering and in the Institute for Research in Electronics and Applied Physics (IREAP) at the University of Maryland—College Park. Her group is engaged in fundamental and applied research in materials for energy harvesting and storage, including the realization of novel microscopy methods for functional imaging.

ACKNOWLEDGMENTS

M.S.L. acknowledges financial support from NSF-ECCS (1610833) and the Center for Research in Extreme Batteries CREB-UMD, and the 2015 RASA award. E.M.T. thanks the 2016–2017 UMD Dean's Dissertation Fellowship, the 2017–2018 Hulka Energy Research Fellowship, and the 2017–2018 All-S.T.A.R. Fellowship. C.G. thanks the 2017–2018 Harry K. Wells Graduate Fellowship. Both E.M.T. and C.G. thank the 2017 UMD graduate school summer research fellowship.

REFERENCES

- (1) Binnig, G.; Rohrer, H.; Gerber, C.; Weibel, E. Surface Studies by Scanning Tunneling Microscopy. *Phys. Rev. Lett.* **1982**, *49*, 57–61.
- (2) Binnig, G.; Quate, C. F.; Gerber, C. Atomic Force Microscope. *Phys. Rev. Lett.* **1986**, *56*, 930–933.
- (3) Giessibl, F. J. Advances in Atomic Force Microscopy. *Rev. Mod. Phys.* **2003**, *75*, 949–983.
- (4) Garcia, R.; Herruzo, E. T. The Emergence of Multifrequency Force Microscopy. *Nat. Nanotechnol.* **2012**, *7*, 217–226.
- (5) Baykara, M. Z.; Schwendemann, T. C.; Altman, E. I.; Schwarz, U. D. Three-Dimensional Atomic Force Microscopy – Taking Surface Imaging to the Next Level. *Adv. Mater.* **2010**, *22*, 2838–2853.
- (6) Tennyson, E. M.; Howard, J. M.; Leite, M. S. Mesoscale Functional Imaging of Materials for Photovoltaics. *ACS Energy Lett.* **2017**, *2*, 1825–1834.
- (7) Green, M. A.; Bremner, S. P. Energy Conversion Approaches and Materials for High-Efficiency Photovoltaics. *Nat. Mater.* **2016**, *16*, 23–34.
- (8) Ulvestad, A.; Singer, A.; Clark, J. N.; Cho, H. M.; Kim, J. W.; Harder, R.; Maser, J.; Meng, Y. S.; Shpyrko, O. G. Topological Defect Dynamics in Operando Battery Nanoparticles. *Science* **2015**, *348*, 1344–1347.
- (9) Kim, Y. C.; Jeon, N. J.; Noh, J. H.; Yang, W. S.; Seo, J.; Yun, J. S.; Ho-Baillie, A.; Huang, S.; Green, M. A.; Seidel, J.; et al. Beneficial Effects of PbI₂ Incorporated in Organo-Lead Halide Perovskite Solar Cells. *Adv. Energy Mater.* **2016**, *6*, 1502104.
- (10) Cox, P. A.; Glaz, M. S.; Harrison, J. S.; Peurifoy, S. R.; Coffey, D. C.; Ginger, D. S. Imaging Charge Transfer State Excitations in Polymer/Fullerene Solar Cells with Time-Resolved Electrostatic Force Microscopy. *J. Phys. Chem. Lett.* **2015**, *6*, 2852–2858.
- (11) Tennyson, E. M.; Garrett, J. L.; Frantz, J. A.; Myers, J. D.; Bekele, R. Y.; Sanghera, J. S.; Munday, J. N.; Leite, M. S. Nanoimaging of Open-Circuit Voltage in Photovoltaic Devices. *Adv. Energy Mater.* **2015**, *5*, 1501142.
- (12) Tuteja, M.; Mei, A. B.; Palekis, V.; Hall, A.; MacLaren, S.; Ferekides, C. S.; Rockett, A. A. CdCl₂ Treatment-Induced Enhanced Conductivity in CdTe Solar Cells Observed Using Conductive Atomic Force Microscopy. *J. Phys. Chem. Lett.* **2016**, *7*, 4962–4967.
- (13) Araki, K.; Ie, Y.; Aso, Y.; Matsumoto, T. Fine Structures of Organic Photovoltaic Thin Films Probed by Frequency-Shift Electrostatic Force Microscopy. *Jpn. J. Appl. Phys.* **2016**, *55*, 070305.
- (14) Matsumura, K.; et al. Characterization of Carrier Concentration in CIGS Solar Cells by Scanning Capacitance Microscopy. *Meas. Sci. Technol.* **2014**, *25*, 044020.
- (15) Garrett, J. L.; Tennyson, E. M.; Hu, M.; Huang, J.; Munday, J. N.; Leite, M. S. Real-Time Nanoscale Open-Circuit Voltage Dynamics of Perovskite Solar Cells. *Nano Lett.* **2017**, *17*, 2554–2560.
- (16) Kelvin, L. On Electric Machines Founded on Induction and Convection. *Philos. Mag.* **1898**, *46*, 66–73.
- (17) Nonnenmacher, M.; O'Boyle, M. P.; Wickramasinghe, H. K. Kelvin Probe Force Microscopy. *Appl. Phys. Lett.* **1991**, *58*, 2921–2923.
- (18) Melitz, W.; Shen, J.; Kummel, A. C.; Lee, S. Kelvin Probe Force Microscopy and its Application. *Surf. Sci. Rep.* **2011**, *66*, 1–27.
- (19) Sadewasser, S.; Glatzel, T.; Schuler, S.; Nishiwaki, S.; Kaigawa, R.; Lux-Steiner, M. C. Kelvin Probe Force Microscopy for the Nano

Scale Characterization of Chalcopyrite Solar Cell Materials and Devices. *Thin Solid Films* **2003**, *431*–432, 257–261.

(20) Melitz, W.; Shen, J.; Lee, S.; Lee, J. S.; Kummel, A. C.; Droopad, R.; Yu, E. T. Scanning Tunneling Spectroscopy and Kelvin Probe Force Microscopy Investigation of Fermi Energy Level Pinning Mechanism on InAs and InGaAs Clean Surfaces. *J. Appl. Phys.* **2010**, *108*, 023711.

(21) Yogev, S.; Matsubara, R.; Nakamura, M.; Zschieschang, U.; Klauk, H.; Rosenwaks, Y. Fermi Level Pinning by Gap States in Organic Semiconductors. *Phys. Rev. Lett.* **2013**, *110*, 036803.

(22) Zhang, Y.; Ziegler, D.; Salmeron, M. Charge Trapping States at the SiO₂–Oligothiophene Monolayer Interface in Field Effect Transistors Studied by Kelvin Probe Force Microscopy. *ACS Nano* **2013**, *7*, 8258–8265.

(23) Fernández Garrillo, P. A.; Borowik, Ł.; Caffy, F.; Demadrille, R.; Grévin, B. Photo-Carrier Multi-Dynamical Imaging at the Nanometer Scale in Organic and Inorganic Solar Cells. *ACS Appl. Mater. Interfaces* **2016**, *8*, 31460–31468.

(24) Borowik, Ł.; Lepage, H.; Chevalier, N.; Mariolle, D.; Renault, O. Measuring the Lifetime of Silicon Nanocrystal Solar Cell Photo-carriers by Using Kelvin Probe Force Microscopy and X-ray Photoelectron Spectroscopy. *Nanotechnology* **2014**, *25*, 265703.

(25) Takihara, M.; Takahashi, T.; Ujihara, T. Minority Carrier Lifetime in Polycrystalline Silicon Solar Cells Studied by Photoassisted Kelvin Probe Force Microscopy. *Appl. Phys. Lett.* **2008**, *93*, 021902.

(26) Shao, G.; Glaz, M. S.; Ma, F.; Ju, H.; Ginger, D. S. Intensity-Modulated Scanning Kelvin Probe Microscopy for Probing Recombination in Organic Photovoltaics. *ACS Nano* **2014**, *8*, 10799–10807.

(27) Girard, P. Electrostatic Force Microscopy: Principles and some Applications to Semiconductors. *Nanotechnology* **2001**, *12*, 485–490.

(28) Hong, J. W.; Noh, K. H.; Park, S.-i.; Kwun, S. I.; Khim, Z. G. Surface Charge Density and Evolution of Domain Structure in Triglycine Sulfate Determined by Electrostatic-Force Microscopy. *Phys. Rev. B: Condens. Matter Mater. Phys.* **1998**, *58*, 5078–5084.

(29) Sangwan, V. K.; Jariwala, D.; Kim, I. S.; Chen, K.-S.; Marks, T. J.; Lauhon, L. J.; Hersam, M. C. Gate-Tunable Memristive Phenomena Mediated by Grain Boundaries in Single-Layer MoS₂. *Nat. Nanotechnol.* **2015**, *10*, 403–406.

(30) Coffey, D. C.; Ginger, D. S. Time-Resolved Electrostatic Force Microscopy of Polymer Solar Cells. *Nat. Mater.* **2006**, *5*, 735–740.

(31) Jaquith, M.; Muller, E. M.; Marohn, J. A. Time-Resolved Electric Force Microscopy of Charge Trapping in Polycrystalline Pentacene. *J. Phys. Chem. B* **2007**, *111*, 7711–7714.

(32) Kutes, Y.; Zhou, Y.; Bosse, J. L.; Steffes, J.; Padture, N. P.; Huey, B. D. Mapping the Photoresponse of CH₃NH₃PbI₃ Hybrid Perovskite Thin Films at the Nanoscale. *Nano Lett.* **2016**, *16*, 3434–3441.

(33) Leblebici, S. Y.; Leppert, L.; Li, Y.; Reyes-Lillo, S. E.; Wickenburg, S.; Wong, E.; Lee, J.; Melli, M.; Ziegler, D.; Angell, D. K.; et al. Facet-Dependent Photovoltaic Efficiency Variations in Single Grains of Hybrid Halide Perovskite. *Nat. Energy* **2016**, *1*, 16093.

(34) Li, J.-J.; Ma, J.-Y.; Ge, Q.-Q.; Hu, J.-S.; Wang, D.; Wan, L.-J. Microscopic Investigation of Grain Boundaries in Organolead Halide Perovskite Solar Cells. *ACS Appl. Mater. Interfaces* **2015**, *7*, 28518–28523.

(35) Nguyen, B. P.; et al. Trapping Charges at Grain Boundaries and Degradation of CH₃NH₃Pb(I_{1-x}Br_x)₃ Perovskite Solar Cells. *Nanotechnology* **2017**, *28*, 315402.

(36) Luria, J.; Kutes, Y.; Moore, A.; Zhang, L.; Stach, E. A.; Huey, B. D. Charge Transport in CdTe Solar Cells Revealed by Conductive Tomographic Atomic Force Microscopy. *Nat. Energy* **2016**, *1*, 16150.

(37) Muhunthan, N.; Singh, O. P.; Toutam, V.; Singh, V. N. Electrical Characterization of Grain Boundaries of CZTS Thin Films using Conductive Atomic Force Microscopy Techniques. *Mater. Res. Bull.* **2015**, *70*, 373–378.

(38) Bull, T. A.; Pingree, L. S. C.; Jenekhe, S. A.; Ginger, D. S.; Luscombe, C. K. The Role of Mesoscopic PCBM Crystallites in Solvent Vapor Annealed Copolymer Solar Cells. *ACS Nano* **2009**, *3*, 627–636.

(39) Dang, X.-D.; Tamayo, A. B.; Seo, J.; Hoven, C. V.; Walker, B.; Nguyen, T.-Q. Nanostructure and Optoelectronic Characterization of Small Molecule Bulk Heterojunction Solar Cells by Photoconductive Atomic Force Microscopy. *Adv. Funct. Mater.* **2010**, *20*, 3314–3321.

(40) Tsoi, W. C.; Nicholson, P. G.; Kim, J. S.; Roy, D.; Burnett, T. L.; Murphy, C. E.; Nelson, J.; Bradley, D. D. C.; Kim, J.-S.; Castro, F. A. Surface and Subsurface Morphology of Operating Nanowire:Fullerene Solar Cells Revealed by Photoconductive-AFM. *Energy Environ. Sci.* **2011**, *4*, 3646–3651.

(41) Guide, M.; Dang, X.-D.; Nguyen, T.-Q. Nanoscale Characterization of Tetrabenzoporphyrin and Fullerene-Based Solar Cells by Photoconductive Atomic Force Microscopy. *Adv. Mater.* **2011**, *23*, 2313–2319.

(42) Letertre, L.; Douhéret, O.; Bougouma, M.; Doneux, T.; Lazzaroni, R.; Buess-Herman, C.; Leclère, P. Nanoscale Study of MoSe₂/Poly(3-Hexylthiophene) Bulk Heterojunctions for Hybrid Photovoltaic Applications. *Sol. Energy Mater. Sol. Cells* **2016**, *145*, 116–125.

(43) McCandless, B. E.; Youm, I.; Birkmire, R. W. Optimization of Vapor Post-Deposition Processing for Evaporated CdS/CdTe Solar Cells. *Prog. Photovoltaics* **1999**, *7*, 21–30.

(44) Major, J. D. Grain Boundaries in CdTe Thin Film Solar Cells: A Review. *Semicond. Sci. Technol.* **2016**, *31*, 093001.

(45) Paudel, N. R.; Young, M.; Roland, P. J.; Ellingson, R. J.; Yan, Y.; Compaan, A. D. Post-Deposition Processing Options for High-Efficiency Sputtered CdS/CdTe Solar Cells. *J. Appl. Phys.* **2014**, *115*, 064502.

(46) Kobayashi, K.; Yamada, H.; Matsushige, K. Dopant Profiling on Semiconducting Sample by Scanning Capacitance Force Microscopy. *Appl. Phys. Lett.* **2002**, *81*, 2629–2631.

(47) Visoly-Fisher, I.; Cohen, S. R.; Cahen, D. Direct Evidence for Grain-Boundary Depletion in Polycrystalline CdTe from Nanoscale-Resolved Measurements. *Appl. Phys. Lett.* **2003**, *82*, 556–558.

(48) Fujita, T.; et al. Analytical Procedure for Experimental Quantification of Carrier Concentration in Semiconductor Devices by Using Electric Scanning Probe Microscopy. *Meas. Sci. Technol.* **2014**, *25*, 044021.

(49) Nicoara, N.; Lepetit, T.; Arzel, L.; Harel, S.; Barreau, N.; Sadewasser, S. Effect of the KF Post-Deposition Treatment on Grain Boundary Properties in Cu(In, Ga)Se₂ Thin Films. *Sci. Rep.* **2017**, *7*, 41361.

(50) Dazzi, A.; Prater, C. B. AFM-IR: Technology and Applications in Nanoscale Infrared Spectroscopy and Chemical Imaging. *Chem. Rev.* **2017**, *117*, 5146–5173.

(51) Yoon, S. J.; Kuno, M.; Kamat, P. V. Shift Happens. How Halide Ion Defects Influence Photoinduced Segregation in Mixed Halide Perovskites. *ACS Energy Lett.* **2017**, *2*, 1507–1514.

(52) Chae, J.; Dong, Q.; Huang, J.; Centrone, A. Chloride Incorporation Process in CH₃NH₃PbI_{3-x}Cl_x Perovskites via Nanoscale Bandgap Maps. *Nano Lett.* **2015**, *15*, 8114–8121.

(53) Nowak, D.; Morrison, W.; Wickramasinghe, H. K.; Jahng, J.; Potma, E.; Wan, L.; Ruiz, R.; Albrecht, T. R.; Schmidt, K.; Frommer, J.; et al. Nanoscale Chemical Imaging by Photoinduced Force Microscopy. *Sci. Adv.* **2016**, *2*, e1501571.

(54) Wang, X.; Zhang, D.; Braun, K.; Egelhaaf, H.-J.; Brabec, C. J.; Meixner, A. J. High-Resolution Spectroscopic Mapping of the Chemical Contrast from Nanometer Domains in P3HT:PCBM Organic Blend Films for Solar-Cell Applications. *Adv. Funct. Mater.* **2010**, *20*, 492–499.

(55) Polizzotti, A.; Repins, I. L.; Noufi, R.; Wei, S.-H.; Mitzi, D. B. The State and Future Prospects of Kesterite Photovoltaics. *Energy Environ. Sci.* **2013**, *6*, 3171–3182.

(56) Ghosh, S.; Kouamé, N. A.; Ramos, L.; Remita, S.; Dazzi, A.; Deniset-Besseau, A.; Beaunier, P.; Goubard, F.; Aubert, P.-H.; Remita, H. Conducting Polymer Nanostructures for Photocatalysis Under Visible Light. *Nat. Mater.* **2015**, *14*, 505–511.

(57) Schmid, T.; Opilik, L.; Blum, C.; Zenobi, R. Nanoscale Chemical Imaging Using Tip-Enhanced Raman Spectroscopy: A Critical Review. *Angew. Chem., Int. Ed.* **2013**, *52*, 5940–5954.

- (58) Zaleski, S.; Wilson, A. J.; Mattei, M.; Chen, X.; Goubert, G.; Cardinal, M. F.; Willets, K. A.; Van Duyne, R. P. Investigating Nanoscale Electrochemistry with Surface- and Tip-Enhanced Raman Spectroscopy. *Acc. Chem. Res.* **2016**, *49*, 2023–2030.
- (59) Jiang, N.; Kurouski, D.; Pozzi, E. A.; Chiang, N.; Hersam, M. C.; Van Duyne, R. P. Tip-Enhanced Raman Spectroscopy: From Concepts to Practical Applications. *Chem. Phys. Lett.* **2016**, *659*, 16–24.
- (60) Nicholson, P. G.; Castro, F. A. Organic Photovoltaics: Principles and Techniques for Nanometre Scale Characterization. *Nanotechnology* **2010**, *21*, 492001.
- (61) Yeo, B.-S.; Stadler, J.; Schmid, T.; Zenobi, R.; Zhang, W. Tip-Enhanced Raman Spectroscopy – Its Status, Challenges and Future Directions. *Chem. Phys. Lett.* **2009**, *472*, 1–13.
- (62) Rajapaksa, I.; Uenal, K.; Wickramasinghe, H. K. Image Force Microscopy of Molecular Resonance: A Microscope Principle. *Appl. Phys. Lett.* **2010**, *97*, 073121.
- (63) Rajapaksa, I.; Kumar Wickramasinghe, H. Raman Spectroscopy and Microscopy Based on Mechanical Force Detection. *Appl. Phys. Lett.* **2011**, *99*, 161103.
- (64) Jahng, J.; Fishman, D. A.; Park, S.; Nowak, D. B.; Morrison, W. A.; Wickramasinghe, H. K.; Potma, E. O. Linear and Nonlinear Optical Spectroscopy at the Nanoscale with Photoinduced Force Microscopy. *Acc. Chem. Res.* **2015**, *48*, 2671–2679.
- (65) Slotcavage, D. J.; Karunadasa, H. I.; McGehee, M. D. Light-Induced Phase Segregation in Halide-Perovskite Absorbers. *ACS Energy Lett.* **2016**, *1*, 1199–1205.
- (66) Dazzi, A.; Prazeres, R.; Glotin, F.; Ortega, J. M. Local Infrared Microspectroscopy with Subwavelength Spatial Resolution with an Atomic Force Microscope Tip used as a Photothermal Sensor. *Opt. Lett.* **2005**, *30*, 2388–2390.
- (67) Cho, H.; et al. Improved Atomic Force Microscope Infrared Spectroscopy for Rapid Nanometer-Scale Chemical Identification. *Nanotechnology* **2013**, *24*, 444007.
- (68) Dazzi, A.; Glotin, F.; Carminati, R. Theory of Infrared Nanospectroscopy by Photothermal Induced Resonance. *J. Appl. Phys.* **2010**, *107*, 124519.
- (69) Felts, J. R.; Kjoller, K.; Lo, M.; Prater, C. B.; King, W. P. Nanometer-Scale Infrared Spectroscopy of Heterogeneous Polymer Nanostructures Fabricated by Tip-Based Nanofabrication. *ACS Nano* **2012**, *6*, 8015–8021.
- (70) Lahiri, B.; Holland, G.; Centrone, A. Chemical Imaging: Chemical Imaging Beyond the Diffraction Limit: Experimental Validation of the PTIR Technique. *Small* **2013**, *9*, 439–445.
- (71) Strelcov, E.; Dong, Q.; Li, T.; Chae, J.; Shao, Y.; Deng, Y.; Gruverman, A.; Huang, J.; Centrone, A. $\text{CH}_3\text{NH}_3\text{PbI}_3$ Perovskites: Ferroelasticity Revealed. *Sci. Adv.* **2017**, *3*, e1602165.
- (72) Gong, C.; Dias, M. R. S.; Wessler, G. C.; Taillon, J. A.; Salamanca-Riba, L. G.; Leite, M. S. Near-Field Optical Properties of Fully Alloyed Noble Metal Nanoparticles. *Adv. Opt. Mater.* **2017**, *5*, 1600568.
- (73) Hecht, B.; Sick, B.; Wild, U. P.; Deckert, V.; Zenobi, R.; Martin, O. J. F.; Pohl, D. W. Scanning Near-Field Optical Microscopy with Aperture Probes: Fundamentals and Applications. *J. Chem. Phys.* **2000**, *112*, 7761–7774.
- (74) Zhang, Y.; Wang, Y.; Xu, Z.-Q.; Liu, J.; Song, J.; Xue, Y.; Wang, Z.; Zheng, J.; Jiang, L.; Zheng, C.; et al. Reversible Structural Swell–Shrink and Recoverable Optical Properties in Hybrid Inorganic–Organic Perovskite. *ACS Nano* **2016**, *10*, 7031–7038.
- (75) Bao, W.; Melli, M.; Caselli, N.; Riboli, F.; Wiersma, D. S.; Staffaroni, M.; Choo, H.; Ogletree, D. F.; Aloni, S.; Bokor, J.; et al. Mapping Local Charge Recombination Heterogeneity by Multidimensional Nanospectroscopic Imaging. *Science* **2012**, *338*, 1317–21.
- (76) Leite, M. S.; Abashin, M.; Lezec, H. J.; Gianfrancesco, A. G.; Talin, A. A.; Zhitenev, N. B. Nanoscale Imaging of Photocurrent and Efficiency in CdTe Solar Cells. *ACS Nano* **2014**, *8*, 11883–11890.
- (77) Leite, M. S.; Abashin, M.; Lezec, H. J.; Gianfrancesco, A. G.; Talin, A. A.; Zhitenev, N. B. Mapping the Local Photoelectronic Properties of Polycrystalline Solar Cells Through High Resolution Laser-Beam-Induced Current Microscopy. *IEEE J. Photovolt.* **2014**, *4*, 311–316.
- (78) Greenaway, A. L.; Sharps, M. C.; Boucher, J. W.; Strange, L. E.; Kast, M. G.; Aloni, S.; Boettcher, S. W. Selective Area Epitaxy of GaAs Microstructures by Close-Spaced Vapor Transport for Solar Energy Conversion Applications. *ACS Energy Lett.* **2016**, *1*, 402–408.
- (79) Ritenour, A. J.; Boucher, J. W.; DeLancey, R.; Greenaway, A. L.; Aloni, S.; Boettcher, S. W. Doping and Electronic Properties of GaAs Grown by Close-Spaced Vapor Transport from Powder Sources for Scalable III-V Photovoltaics. *Energy Environ. Sci.* **2015**, *8*, 278–285.
- (80) Paetzold, U. W.; Lehnen, S.; Bittkau, K.; Rau, U.; Carius, R. Nanoscale Observation of Waveguide Modes Enhancing the Efficiency of Solar Cells. *Nano Lett.* **2014**, *14*, 6599–6605.
- (81) Synge, E. H. XXXVIII. A Suggested Method for Extending Microscopic Resolution into the Ultra-Microscopic Region. *Philos. Mag.* **1928**, *6*, 356–362.
- (82) Dürig, U.; Pohl, D. W.; Rohner, F. Near-field Optical-Scanning Microscopy. *J. Appl. Phys.* **1986**, *59*, 3318–3327.
- (83) Lewis, A.; Isaacson, M.; Harootunian, A.; Muray, A. Development of a 500 Å Spatial Resolution Light Microscope. *Ultramicroscopy* **1984**, *13*, 227–231.
- (84) Kim, J.; Song, K.-B. Recent Progress of Nano-Technology with NSOM. *Micron* **2007**, *38*, 409–426.
- (85) Ogletree, D. F.; Schuck, P. J.; Weber-Bargioni, A. F.; Borys, N. J.; Aloni, S.; Bao, W.; Barja, S.; Lee, J.; Melli, M.; Munechika, K.; et al. Revealing Optical Properties of Reduced-Dimensionality Materials at Relevant Length Scales. *Adv. Mater.* **2015**, *27*, 5693–5719.
- (86) Vrućinić, M.; Matthiesen, C.; Sadhanala, A.; Divitini, G.; Cacovich, S.; Dutton, S. E.; Ducati, C.; Atatüre, M.; Snaith, H.; Friend, R. H.; et al. Local Versus Long-Range Diffusion Effects of Photoexcited States on Radiative Recombination in Organic–Inorganic Lead Halide Perovskites. *Adv. Sci.* **2015**, *2*, 1500136.
- (87) Okamoto, K.; Scherer, A.; Kawakami, Y. Near-Field Scanning Optical Microscopic Transient Lens for Carrier Dynamics Study in InGaN/GaN. *Appl. Phys. Lett.* **2005**, *87*, 161104.
- (88) Nakayama, K.; Tanabe, K.; Atwater, H. A. Plasmonic Nanoparticle Enhanced Light Absorption in GaAs Solar Cells. *Appl. Phys. Lett.* **2008**, *93*, 121904.
- (89) Das, D. J.; Shivanna, R.; Narayan, K. S. Photoconductive NSOM for Mapping Optoelectronic Phases in Nanostructures. *Nanophotonics* **2014**, *3*, 19–31.
- (90) Atkin, J. M.; Berweger, S.; Jones, A. C.; Raschke, M. B. Nano-Optical Imaging and Spectroscopy of Order, Phases, and Domains in Complex Solids. *Adv. Phys.* **2012**, *61*, 745–842.
- (91) Bek, A.; Vogelgesang, R.; Kern, K. Apertureless Scanning Near Field Optical Microscope with Sub-10nm Resolution. *Rev. Sci. Instrum.* **2006**, *77*, 043703.
- (92) Green, M. A.; Hishikawa, Y.; Warta, W.; Dunlop, E. D.; Levi, D. H.; Hohl-Ebinger, J.; Ho-Baillie, A. W. Y. Solar Cell Efficiency Tables (Version 50). *Prog. Photovoltaics* **2017**, *25*, 668–676.
- (93) imec.magazine Imec Reports Record Conversion Efficiency of 23.9% on a 4 cm² Perovskite/Silicon Solar Module. <https://www.imec-int.com/en/articles/imec-reports-record-conversion-efficiency-of-23-9-percent-on-a-4cm2-perovskite-silicon-solar-module> (accessed August 19, 2017).
- (94) Grancini, G.; Roldán-Carmona, C.; Zimmermann, I.; Mosconi, E.; Lee, X.; Martineau, D.; Nabey, S.; Oswald, F.; De Angelis, F.; Graetzel, M.; et al. One-Year Stable Perovskite Solar Cells by 2D/3D Interface Engineering. *Nat. Commun.* **2017**, *8*, 15684.
- (95) Saliba, M.; Matsui, T.; Seo, J.-Y.; Domanski, K.; Correa-Baena, J.-P.; Nazeeruddin, M. K.; Zakeeruddin, S. M.; Tress, W.; Abate, A.; Hagfeldt, A.; et al. Cesium-Containing Triple Cation Perovskite Solar Cells: Improved Stability, Reproducibility and High Efficiency. *Energy Environ. Sci.* **2016**, *9*, 1989–1997.
- (96) Beal, R. E.; Slotcavage, D. J.; Leijtens, T.; Bowring, A. R.; Belisle, R. A.; Nguyen, W. H.; Burkhard, G. F.; Hoke, E. T.; McGehee, M. D. Cesium Lead Halide Perovskites with Improved Stability for Tandem Solar Cells. *J. Phys. Chem. Lett.* **2016**, *7*, 746–751.

- (97) Berry, J.; Buonassisi, T.; Egger, D. A.; Hodes, G.; Kronik, L.; Loo, Y.-L.; Lubomirsky, I.; Marder, S. R.; Mastai, Y.; Miller, J. S.; et al. Hybrid Organic-Inorganic Perovskites (HOIPs): Opportunities and Challenges. *Adv. Mater.* **2015**, *27*, 5102–5112.
- (98) Bryant, D.; Aristidou, N.; Pont, S.; Sanchez-Molina, I.; Chotchunangatchaval, T.; Wheeler, S.; Durrant, J. R.; Haque, S. A. Light and Oxygen Induced Degradation Limits the Operational Stability of Methylammonium Lead Triiodide Perovskite Solar Cells. *Energy Environ. Sci.* **2016**, *9*, 1655–1660.
- (99) Yang, D.; Lv, J.; Zhao, X.; Xu, Q.; Fu, Y.; Zhan, Y.; Zunger, A.; Zhang, L. Functionality-Directed Screening of Pb-Free Hybrid Organic-Inorganic Perovskites with Desired Intrinsic Photovoltaic Functionalities. *Chem. Mater.* **2017**, *29*, 524–538.
- (100) Li, L.; Liu, N.; Xu, Z.; Chen, Q.; Wang, X.; Zhou, H. Precise Composition Tailoring of Mixed-Cation Hybrid Perovskites for Efficient Solar Cells by Mixture Design Methods. *ACS Nano* **2017**, *11*, 8804.
- (101) Bergmann, V. W.; Weber, S. A. L.; Javier Ramos, F.; Nazeeruddin, M. K.; Grätzel, M.; Li, D.; Domanski, A. L.; Lieberwirth, I.; Ahmad, S.; Berger, R. Real-Space Observation of Unbalanced Charge Distribution Inside a Perovskite-Sensitized Solar Cell. *Nat. Commun.* **2014**, *5*, 5001.
- (102) Asghar, M. I.; Zhang, J.; Wang, H.; Lund, P. D. Device Stability of Perovskite Solar Cells – A Review. *Renewable Sustainable Energy Rev.* **2017**, *77*, 131–146.
- (103) Park, N.-G.; Grätzel, M.; Miyasaka, T.; Zhu, K.; Emery, K. Towards Stable and Commercially Available Perovskite Solar Cells. *Nat. Energy* **2016**, *1*, 16152.
- (104) Tress, W.; Marinova, N.; Moehl, T.; Zakeeruddin, S. M.; Nazeeruddin, M. K.; Grätzel, M. Understanding the Rate-Dependent J-V Hysteresis, Slow Time Component, and Aging in $\text{CH}_3\text{NH}_3\text{PbI}_3$ Perovskite Solar Cells: the Role of a Compensated Electric Field. *Energy Environ. Sci.* **2015**, *8*, 995–1004.
- (105) Wang, L.; Wang, H.; Wagner, M.; Yan, Y.; Jakob, D. S.; Xu, X. G. Nanoscale Simultaneous Chemical and Mechanical Imaging via Peak Force Infrared Microscopy. *Sci. Adv.* **2017**, *3*, e1700255.
- (106) Fares, R. L.; Webber, M. E. The Impacts of Storing Solar Energy in the Home to Reduce Reliance on the Utility. *Nat. Energy* **2017**, *2*, 17001.
- (107) Liang, K.; Li, L.; Yang, Y. Inorganic Porous Films for Renewable Energy Storage. *ACS Energy Lett.* **2017**, *2*, 373–390.
- (108) Gong, C.; Ruzmetov, D.; Pearce, A.; Ma, D.; Munday, J. N.; Rubloff, G.; Talin, A. A.; Leite, M. S. Surface/Interface Effects on High-Performance Thin-Film All-Solid-State Li-Ion Batteries. *ACS Appl. Mater. Interfaces* **2015**, *7*, 26007–26011.
- (109) Herle, P. S.; Ellis, B.; Coombs, N.; Nazar, L. F. Nano-Network Electronic Conduction in Iron and Nickel Olivine Phosphates. *Nat. Mater.* **2004**, *3*, 147–152.
- (110) Santhanagopalan, D.; Qian, D.; McGilvray, T.; Wang, Z.; Wang, F.; Camino, F.; Graetz, J.; Dudney, N.; Meng, Y. S. Interface Limited Lithium Transport in Solid-State Batteries. *J. Phys. Chem. Lett.* **2014**, *5*, 298–303.
- (111) Leite, M. S.; Ruzmetov, D.; Li, Z.; Bendersky, L. A.; Bartelt, N. C.; Kolmakov, A.; Talin, A. A. Insights into Capacity Loss Mechanisms of All-Solid-State Li-Ion Batteries with Al Anodes. *J. Mater. Chem. A* **2014**, *2*, 20552–20559.
- (112) Whittingham, M. S. Ultimate Limits to Intercalation Reactions for Lithium Batteries. *Chem. Rev.* **2014**, *114*, 11414–11443.
- (113) Sun, Y.-K.; Myung, S.-T.; Park, B.-C.; Prakash, J.; Belharouak, I.; Amine, K. High-Energy Cathode Material for Long-Life and Safe Lithium Batteries. *Nat. Mater.* **2009**, *8*, 320–324.
- (114) Kalinin, S.; Balke, N.; Jesse, S.; Tselev, A.; Kumar, A.; Arruda, T. M.; Guo, S.; Proksch, R. Li-Ion Dynamics and Reactivity on the Nanoscale. *Mater. Today* **2011**, *14*, 548–558.
- (115) Yang, S.; Yan, B.; Lu, L.; Zeng, K. Grain Boundary Effects on Li-Ion Diffusion in a $\text{Li}_{1.2}\text{Co}_{0.13}\text{Ni}_{0.13}\text{Mn}_{0.54}\text{O}_2$ Thin Film Cathode Studied by Scanning Probe Microscopy Techniques. *RSC Adv.* **2016**, *6*, 94000–94009.
- (116) Takahashi, Y.; Kumatani, A.; Munakata, H.; Inomata, H.; Ito, K.; Ino, K.; Shiku, H.; Unwin, P. R.; Korchev, Y. E.; Kanamura, K.; et al. Nanoscale Visualization of Redox Activity at Lithium-Ion Battery Cathodes. *Nat. Commun.* **2014**, *5*, 5450.
- (117) Balke, N.; Jesse, S.; Kim, Y.; Adamczyk, L.; Tselev, A.; Ivanov, I. N.; Dudney, N. J.; Kalinin, S. V. Real Space Mapping of Li-Ion Transport in Amorphous Si Anodes with Nanometer Resolution. *Nano Lett.* **2010**, *10*, 3420–3425.
- (118) Mascaro, A.; Wang, Z.; Hovington, P.; Miyahara, Y.; Paoletta, A.; Garipey, V.; Feng, Z.; Enright, T.; Aiken, C.; Zaghbi, K.; et al. Measuring Spatially Resolved Collective Ionic Transport on Lithium Battery Cathodes Using Atomic Force Microscopy. *Nano Lett.* **2017**, *17*, 4489–4496.
- (119) Williams, C. G.; Edwards, M. A.; Colley, A. L.; Macpherson, J. V.; Unwin, P. R. Scanning Micropipet Contact Method for High-Resolution Imaging of Electrode Surface Redox Activity. *Anal. Chem.* **2009**, *81*, 2486–2495.
- (120) Snowden, M. E.; Güell, A. G.; Lai, S. C. S.; McKelvey, K.; Ebejer, N.; O'Connell, M. A.; Colburn, A. W.; Unwin, P. R. Scanning Electrochemical Cell Microscopy: Theory and Experiment for Quantitative High Resolution Spatially-Resolved Voltammetry and Simultaneous Ion-Conductance Measurements. *Anal. Chem.* **2012**, *84*, 2483–2491.
- (121) Balke, N.; Jesse, S.; Morozovska, A.; Eliseev, E.; Chung, D.; Kim, Y.; Adamczyk, L.; Garcia, R.; Dudney, N.; Kalinin, S. Nanoscale Mapping of Ion Diffusion in a Lithium-Ion Battery Cathode. *Nat. Nanotechnol.* **2010**, *5*, 749–754.
- (122) Chen, Q. N.; Liu, Y.; Liu, Y.; Xie, S.; Cao, G.; Li, J. Delineating Local Electromigration for Nanoscale Probing of Lithium Ion Intercalation and Extraction by Electrochemical Strain Microscopy. *Appl. Phys. Lett.* **2012**, *101*, 063901.
- (123) Banov, B.; Momchilov, A.; Trifonova, A.; Puresheva, B. Comparative Study Between 4-V LiMn_2O_4 , LiCoO_2 and 3-V $\text{Li}_{0.3}\text{MnO}_2$, LiV_3O_8 as Cathode Materials for Li Batteries. In *Materials for Lithium-Ion Batteries*; Julien, C., Stoyanov, Z., Eds.; Springer: The Netherlands, 2000.
- (124) Zhu, J.; Lu, L.; Zeng, K. Nanoscale Mapping of Lithium-Ion Diffusion in a Cathode within an All-Solid-State Lithium-Ion Battery by Advanced Scanning Probe Microscopy Techniques. *ACS Nano* **2013**, *7*, 1666–1675.
- (125) Nonnenmann, S. S.; Kungas, R.; Vohs, J.; Bonnell, D. A. Direct In Situ Probe of Electrochemical Processes in Operating Fuel Cells. *ACS Nano* **2013**, *7*, 6330–6336.
- (126) Carrette, L.; Friedrich, K. A.; Stimming, U. Fuel Cells: Principles, Types, Fuels, and Applications. *ChemPhysChem* **2000**, *1*, 162–193.
- (127) Louie, M. W.; Hightower, A.; Haile, S. M. Nanoscale Electrodes by Conducting Atomic Force Microscopy: Oxygen Reduction Kinetics at the Pt/CsHSO_4 Interface. *ACS Nano* **2010**, *4*, 2811–2821.
- (128) Jiang, S. P. Thermally and Electrochemically Induced Electrode/Electrolyte Interfaces in Solid Oxide Fuel Cells: An AFM and EIS Study. *J. Electrochem. Soc.* **2015**, *162*, F1119–F1128.
- (129) Nasr Eshghinejad, A.; Lei, C.; Esfahani, E. N.; Li, J. Resolving Local Electrochemistry at the Nanoscale via Electrochemical Strain Microscopy: Modeling and Experiments. *ArXiv* **2017**, arXiv:1704.01158v1.
- (130) Park, H.; Li, X.; Lai, S. Y.; Chen, D.; Blinn, K. S.; Liu, M.; Choi, S.; Liu, M.; Park, S.; Bottomley, L. A. Electrostatic Force Microscopic Characterization of Early Stage Carbon Deposition on Nickel Anodes in Solid Oxide Fuel Cells. *Nano Lett.* **2015**, *15*, 6047–6050.
- (131) Adler, S. B. Factors Governing Oxygen Reduction in Solid Oxide Fuel Cell Cathodes. *Chem. Rev.* **2004**, *104*, 4791–4844.
- (132) Garrett, J. L.; Munday, J. N. Fast, High-Resolution Surface Potential Measurements in Air with Heterodyne Kelvin Probe Force Microscopy. *Nanotechnology* **2016**, *27*, 245705.
- (133) Collins, L.; Ahmadi, M.; Wu, T.; Hu, B.; Kalinin, S. V.; Jesse, S. Breaking the Time Barrier in Kelvin Probe Force Microscopy: Fast

Free Force Reconstruction Using the G-Mode Platform. *ACS Nano* **2017**, *11*, 8717–8729.

(134) Miyahara, Y.; Grutter, P. Force-Gradient Sensitive Kelvin Probe Force Microscopy by Dissipative Electrostatic Force Modulation. *Appl. Phys. Lett.* **2017**, *110*, 163103.

(135) Kim, J. B.; Chang, W. S. Design and Fabrication of a Tip-on-Aperture Probe for Resolution Enhancement of Optical Patterning. *Microelectron. Eng.* **2016**, *151*, 24–29.

(136) Huth, F.; Chuvilin, A.; Schnell, M.; Amenabar, I.; Krutokhvostov, R.; Lopatin, S.; Hillenbrand, R. Resonant Antenna Probes for Tip-Enhanced Infrared Near-Field Microscopy. *Nano Lett.* **2013**, *13*, 1065–1072.

(137) Greenaway, A. L.; Boucher, J. W.; Oener, S. Z.; Funch, C. J.; Boettcher, S. W. Low-Cost Approaches to III–V Semiconductor Growth for Photovoltaic Applications. *ACS Energy Lett.* **2017**, *2*, 2270–2282.

(138) Moutinho, H. R.; Dhere, R. G.; Jiang, C. S.; Yan, Y. F.; Albin, D. S.; Al-Jassim, M. M. Investigation of Potential and Electric Field Profiles in Cross Sections of CdTe/CdS Solar Cells Using Scanning Kelvin Probe Microscopy. *J. Appl. Phys.* **2010**, *108*, 074503.

(139) Han, F.; Zhu, Y.; He, X.; Mo, Y.; Wang, C. Electrochemical Stability of $\text{Li}_{10}\text{GeP}_2\text{S}_{12}$ and $\text{Li}_7\text{La}_3\text{Zr}_2\text{O}_{12}$ Solid Electrolytes. *Adv. Energy Mater.* **2016**, *6*, 1501590.

(140) Lu, L.; Han, X.; Li, J.; Hua, J.; Ouyang, M. A Review on the Key Issues for Lithium-Ion Battery Management in Electric Vehicles. *J. Power Sources* **2013**, *226*, 272–288.

(141) Morris, M. A.; An, H.; Lutkenhaus, J. L.; Epps, T. H. Harnessing the Power of Plastics: Nanostructured Polymer Systems in Lithium-Ion Batteries. *ACS Energy Lett.* **2017**, *2*, 1919–1936.

(142) Tamura, N.; MacDowell, A.; Spolenak, R.; Valek, B.; Bravman, J.; Brown, W.; Celestre, R.; Padmore, H.; Batterman, B.; Patel, J. Scanning X-Ray Microdiffraction with Submicrometer White Beam for Strain/Stress and Orientation Mapping in Thin Films. *J. Synchrotron Radiat.* **2003**, *10*, 137–143.